High order resolution of the Maxwell–Fokker–Planck–Landau model intended for ICF applications

Roland Duclous [a,*], Bruno Dubroca [a], Francis Filbet [b], Vladimir Tikhonchuk [c]

[a] Université Bordeaux I, UMR CELIA CEA, CNRS et Institut de Mathématiques de Bordeaux, 351, Cours de la Libération, F-33405 Talence Cedex, France
[b] Université Lyon, Université Lyon1, INSAL, ECL UMR 5208 – Institut Camille Jordan, 43, Boulevard du 11 Novembre 1918, F-69622 Villeurbanne Cedex, France
[c] Université Bordeaux I, UMR CELIA CEA, CNRS, 351, Cours de la Libération, F-33405 Talence Cedex, France

ARTICLE INFO

ABSTRACT

A high order, deterministic direct numerical method is proposed for the non-relativistic $2D_\mathbf{x} \times 3D_\mathbf{v}$ Vlasov–Maxwell system, coupled with Fokker–Planck–Landau collision operators. The magnetic field is perpendicular to the $2D_\mathbf{x}$ plane surface of computation, whereas the electric fields occur in this plane. Such a system is devoted to modelling of electron transport and energy deposition in the general frame of Inertial Confinement Fusion applications. It is able to describe the kinetics of the plasma electrons in the nonlocal equilibrium regime, and permits to consider a large anisotropy degree of the distribution function. We develop specific methods and approaches for validation, that might be used in other fields where couplings between equations, multiscale physics, and high dimensionality are involved. Fast algorithms are employed, which makes this direct approach computationally affordable for simulations of hundreds of collisional times.

1. Introduction

In the context of interactions between intense, short laser pulses and solid targets [1] or Inertial Confinement Fusion (ICF) schemes [2,3], the electron energy transport is an important issue. In this latter field of applications (ICF), it determines the efficiency of plasma heating and the possibility to achieve the fusion conditions. The appropriate scales under consideration here are about one hundred mean free paths for the typical spatial sizes, and several hundreds of collisional times.

Several key features should be accounted for. First of all, in typical ICF configurations, a significant amount of energetic electrons have a large mean free path, exceeding the characteristic gradient length of the temperature and the density: the particle motion exhibits strong nonlocal features. Moreover, a wide range of collisional regimes should be dealt with to describe the propagation and the slowing down of energetic electrons from the underdense corona of the target to its dense and compressed core. The collisions are important even if the beam particles themselves are collisionless [2]: these particles, when propagating in a plasma, trigger a return current that neutralizes the incident one. This return current is determined by collisions of thermal, background electrons. The structure of the generated electron distribution function is then often anisotropic, with a strongly intercorrelated two population structure. For a non-relativistic laser intensity, smaller than 10^{18} W cm^{-2}, a small angle description for collisions between the two populations is well-suited, leading to the classical Fokker–Planck–Landau collision model. The Coulomb potential involves multiple collisions with small energy exchanges between particles, so that the Landau form of the Fokker–Planck operator is required here. Such a configuration with two counterstreaming beams typically leads to the development of microscopic instabilities that can modify strongly the beam

---

* Corresponding author.
  E-mail addresses: duclous@math.u-bordeaux1.fr (R. Duclous), dubroca@math.u-bordeaux1.fr (B. Dubroca), filbet@math.univ-lyon1.fr (F. Filbet), tikhonchuk@celia.u-bordeaux1.fr (V. Tikhonchuk).

propagation. We refer to the two-stream and filamentation instabilities, where the wave vector of the perturbation is respectively parallel and perpendicular to the direction of the incident beam [4,5]. A self-consistent description of electromagnetic fields is then required to describe the plasma behavior and associated instabilities. Furthermore, in the process of plasma heating, strong magnetic fields are generated at intensity that can reach a MegaGauss scale and may affect the energy transport [6–8]. The sources of magnetic field generation include, on the one hand, the effects of the rotational part of the electron pressure, which is a cross gradient $\nabla T \times \nabla n$ effect, and, on the other hand, the exponential growth of perturbations of an anisotropic distribution function (Weibel instability). These electromagnetic processes can be strongly coupled with non-local effects [9,10].

The plasma model studied in this paper is based on the non-relativistic Vlasov–Maxwell equations, coupled with Fokker–Planck–Landau collision operators. It corresponds to the listed requirements that are relevant for the standard ICF approach with a central point ignition. At higher laser intensities corresponding to the fast ignition approach for ICF, a relativistic treatment should be considered [2,11], and collision operators with a large energy exchange are required. Here, the production of secondary fast electrons proves to be non-negligible, particularly in dense plasmas.

There are several numerical methods that treat the Vlasov–Maxwell model together with Fokker–Planck–Landau type operators. Among them, the collisional Particle-In-Cell (PIC) method has been originally designed to describe accurately collective effects, it gives satisfying results in a limited range of collisional regimes. However, it suffers from the "finite grid instability", that involves numerical heating. Also the statistical noise and a low resolution of the electron distribution function by PIC solvers generally lead to an inaccurate treatment of collisions, particularly when dealing with low temperature and high density plasmas. In the high density regions (hundreds of critical densities), the computational resources needed by the PIC method become currently excessive. Recent collisional PIC solvers [12] rely on the weighted macro-particles to attain high densities, together with high order numerical schemes, to reduce the numerical heating. Another type of widely used methods consists in the expansion of the angular dependance of the distribution function in a series of Legendre polynomials or the spherical harmonics, retaining a limited number of lowest order terms [13,14,2,15,16]. However, this approach cannot apply to a situation that is relevant to the ICF fast ignition, where a collisionless beam-like fast electron population is coupled with a collision dominated thermal population. Also, the study of laser-driven parametric instabilities require an accurate description of collective effects, together with a collisional treatment, in the regions close to the critical density.

Here, we propose a different and complementary approach, that could potentially address these complicated situations. It consists in approximating the full model by a direct deterministic numerical method. Such a method does not involve any perturbative expansion or linearization of the distribution function around an equilibrium state, to obtain reduced and tractable collision operators. It discretizes directly the initial set of equations and enables to preserve at the discrete level the physical invariants of the model (the positivity of the distribution function, the conservation of total mass and total energy, the entropy decreasing behavior, etc). Many deterministic schemes of this type have already been considered for homogeneous Fokker–Planck type operators [17–21]. The nonhomogeneous case, that includes the transport part (see [22] for a comparison between Eulerian Vlasov solvers), involves a large computational complexity that can only be reduced with fast algorithms. Multipole expansion [23] and multigrid [19] techniques, as well as fast spectral methods [20,24], have been applied to the Landau equation. For computational complexity constraints, very few results on the accuracy of these methods are known in the nonhomogeneous case [25,24], particularly when the coupling with magnetic fields is considered [26].

On the one hand for the transport part discretization, our starting point is a second order finite volume scheme introduced in [25]. Its main feature is that it preserves exactly the discrete energy when slope limiters are not active. Here, we introduce additional dissipation on these limiters in order to successfully address the two-stream instability test case. Moreover, we will underline the important role of the limitation procedure for the accuracy, on the second order scheme. This scheme is compared in this test case with a fourth order MUSCL scheme [27], with a limitation ensuring the positivity of the distribution function [28]. A similar approach, with the introduction of a fourth order scheme for transport to avoid numerical heating, has already been proposed in the context of PIC solvers [12].

On the other hand, the discretization of the Maxwell equations is performed with a Crank–Nicholson method, allowing the time steps to be of the order of the collision time. It is designed to preserve the discrete total electromagnetic energy, which is an important issue when we consider the coupling between the Vlasov equation and the Maxwell system to capture accurately energy deposition phenomenon. Finally, for the Landau operator a fast multigrid technique is used that proves to be accurate in a wide range of collisional regimes. Moreover, the use of domain decomposition techniques and distributed memory MPI standard on the space domain leads to affordable computational cost, and to the treatment of time dependent, $2D_{\mathbf{x}} \times 3D_{\mathbf{v}}$ problems.

The paper is organized as follows. First, we present the model and its properties in Section 2. Then we discuss the numerical schemes for the transport part, their properties, and propose several numerical tests (Sections 3 and 4). In Section 5, the discretization for the collision operators is treated and we finally present physical test cases $1D_{\mathbf{x}} \times 3D_{\mathbf{v}}$ and $2D_{\mathbf{x}} \times 3D_{\mathbf{v}}$ that show the accuracy of the present algorithm (Section 6).

2. The kinetic model

Two particle species (ions and electrons) are considered: ions are supposed to be fixed assuming an electron–ion mass ratio $m_e/m_i \ll 1$, whereas the evolution of electrons is described by a distribution function $f_e(t, \mathbf{x}, \mathbf{v})$ where for the more

general case $(\mathbf{x}, \mathbf{v}) \in \Omega \times \mathbb{R}^3$, with $\Omega \subset \mathbb{R}^3$. The non-relativistic Vlasov equation with Fokker–Planck–Landau (FPL) collision operator is given by

$$\frac{\partial f_e}{\partial t} + \nabla_\mathbf{x} \cdot (\mathbf{v} f_e) + \frac{q_e}{m_e} \nabla_\mathbf{v} \cdot ((\mathbf{E} + \mathbf{v} \times \mathbf{B}) f_e) = C_{e,e}(f_e, f_e) + C_{e,i}(f_e), \tag{1}$$

where $q_e = -e$ is the charge of an electron and m_e is the mass of an electron. On the one hand, electromagnetic fields $(\mathbf{E}, \mathbf{B})$ are given by the classical Maxwell system

$$\begin{cases} \frac{\partial \mathbf{E}}{\partial t} - c^2 \nabla_\mathbf{x} \times \mathbf{B} = -\frac{\mathbf{J}}{\epsilon_0}, \\ \frac{\partial \mathbf{B}}{\partial t} + \nabla_\mathbf{x} \times \mathbf{E} = 0, \end{cases} \tag{2}$$

where ϵ_0 represents the permittivity of vacuum and c is the speed of light. The current density is given by

$$\mathbf{J}(t, \mathbf{x}) = q_e \sum_{\mathbb{R}^3} f_e(t, \mathbf{x}, \mathbf{v}) \mathbf{v} \, \mathbf{dv}.$$

Moreover, Maxwell system's is supplemented by Gauss law's

$$\nabla_\mathbf{x} \cdot \mathbf{E} = \frac{\rho}{\epsilon_0}, \quad \nabla_\mathbf{x} \cdot \mathbf{B} = 0, \tag{3}$$

where ρ is the charge density:

$$\rho = q_e(n_e - n_o) = q_e \left(\sum_{\mathbb{R}^3} f_e(t, \mathbf{x}, \mathbf{v}) \mathbf{dv} - n_0 \right),$$

and n_0/Z is the initial ion density.

In this model, the Vlasov equation stands for the invariance of the distribution function along the particles trajectories under the effects of electromagnetic fields $\mathbf{E}$ and $\mathbf{B}$. The Vlasov transport terms, in the left-hand side of Eq. (1), are written in their conservative form, but they can also be written in an equivalent non-conservative form, while the Maxwell equations (2), (3) provide with a complete self-consistent description of electromagnetic fields. The coupling between both is performed *via* the Lorentz force term $\mathbf{E} + \mathbf{v} \times \mathbf{B}$ in the Vlasov equation, and the current source terms in the Maxwell equations.

On the other hand, in Eq. (1), the right-hand side represents collisions between particles, which only act on the velocity variable (the $\mathbf{x}$ variable will be dropped). The FPL operator $C_{e,e}(f_e, f_e)$ stands for the electron–electron collision operator

$$C_{e,e}(f_e, f_e) = \frac{e^4 \ln \Lambda}{8 \pi \epsilon_0^2 m_e^2} \nabla_\mathbf{v} \cdot \left(\sum_{\mathbb{R}^3} \Phi(\mathbf{v} - \mathbf{v}')[f_e(\mathbf{v}') \nabla_\mathbf{v} f_e(\mathbf{v}) - f_e(\mathbf{v}) \nabla'_\mathbf{v} f_e(\mathbf{v}')] \mathbf{dv}' \right), \tag{4}$$

whereas $C_{e,i}(f_e)$ is the electron–ion collision operator

$$C_{e,i}(f_e) = \frac{Z n_0 e^4 \ln \Lambda}{8 \pi \epsilon_0^2 m_e^2} \nabla_\mathbf{v} \cdot [\Phi(\mathbf{v}) \nabla_\mathbf{v} f_e(\mathbf{v})], \tag{5}$$

where $\ln \Lambda$ is the Coulomb logarithm, which is supposed to be constant over the domain and $\Phi(\mathbf{u})$ is an operator acting on the relative velocity $\mathbf{u}$

$$\Phi(\mathbf{u}) = \frac{\|\mathbf{u}\|^2 \mathrm{Id} - \mathbf{u} \otimes \mathbf{u}}{\|\mathbf{u}\|^3}. \tag{6}$$

The FPL operator is used to describe elastic, binary collisions between charged particles, with the long-range Coulomb interaction potential. Classical but important properties of the system (1)–(3) together with operators (4) and (5), are briefly recalled. For detailed proofs, we refer to [25,29]. As we assume ions to be fixed, the FPL operator can then be simplified for electron–ion collisions [25], and reduced to the Lorentz approximation. We refer to [30] for a physical derivation.

2.1. Kinetic equation with self-consistent electromagnetic fields

In this section, collision operators are neglected and we only consider a periodic or infinite space domain. The Vlasov–Maxwell system (1)–(3) with a zero right-hand side is strictly equivalent to (1) and (2) provided the Gauss's laws (3) are initially satisfied. This gives a compatibility condition at initial time.

The mass and momentum are preserved with respect to time for the Vlasov–Maxwell system, *i.e.* system (1) and (2) without collision operators

$$\frac{d}{dt} \sum_{\mathbb{R}^3 \times \mathbb{R}^3} f_e(t, \mathbf{x}, \mathbf{v}) \begin{pmatrix} 1 \\ \mathbf{v} \end{pmatrix} \mathbf{dx} \, \mathbf{dv} = 0, \quad t \geqslant 0.$$

Moreover, the conservation of energy can be proved for the Vlasov–Maxwell system by multiplying Eq. (1) by $m_e \|\mathbf{v}\|^2 / 2$ and integrating it in the velocity space. It gives after an integration by parts

$$\frac{1}{2}\frac{d}{dt}\int_{\mathbb{R}^3}\left\{\epsilon_0\|\mathbf{E}(t,\mathbf{x})\|^2 + \frac{1}{\mu_0}\|\mathbf{B}(t,\mathbf{x})\|^2 + \int_{\mathbb{R}^3} m_e\|\mathbf{v}\|^2 f_e(t,\mathbf{x},\mathbf{v})\mathbf{dv}\right\}\mathbf{dx} = 0, \quad t \geqslant 0,$$

with $c^2\epsilon_0\mu_0 = 1$. The Vlasov–Maxwell system also conserves the kinetic entropy

$$\frac{d}{dt}H(t) = \frac{d}{dt}\int_{\mathbb{R}^3 \times \mathbb{R}^3} f_e(t,\mathbf{x},\mathbf{v}) \log(f_e(t,\mathbf{x},\mathbf{v}))\mathbf{dx}\,\mathbf{dv} = 0, \quad t \geqslant 0.$$

2.2. Collision operators

The FPL operator is used to describe binary elastic collisions between electrons. Its algebraic structure is similar to the Boltzmann operator, in that it satisfies the conservation of mass, momentum and energy

$$\int_{\mathbb{R}^3} C_{e,e}(f_e,f_e)(\mathbf{v})\begin{pmatrix}1\\\mathbf{v}\\\|\mathbf{v}\|^2\end{pmatrix}\mathbf{dv} = 0, \quad t \geqslant 0.$$

Moreover, the entropy is decreasing with respect to time

$$\frac{dH}{dt}(t) = \frac{d}{dt}\int_{\mathbb{R}^3} f_e(\mathbf{v},t) \log(f_e(\mathbf{v},t))\mathbf{dv} \leqslant 0, \quad t \geqslant 0.$$

The equilibrium states of the FPL operator, *i.e.* the set of distribution functions in the kernel of $C_{e,e}(f_e,f_e)$, are given by the Maxwellian distribution functions

$$\mathcal{M}_{n_e,\mathbf{u_e},T_e}(\mathbf{v}) = n_e\left(\frac{m_e}{2\pi T_e}\right)^{3/2} \exp\left(-m_e\frac{\|\mathbf{v}-\mathbf{u_e}\|^2}{2T_e}\right),$$

where n_e is the density, $\mathbf{u_e}$ is the mean velocity and T_e is the temperature, defined as

$$\begin{cases} n_e = \int_{\mathbb{R}^3} f_e(\mathbf{v})\mathbf{dv},\\ \mathbf{u_e} = \frac{1}{n_e}\int_{\mathbb{R}^3} f_e(\mathbf{v})\mathbf{v}\,\mathbf{dv},\\ T_e = \frac{m_e}{3n_e}\int_{\mathbb{R}^3} f_e(\mathbf{v})\|\mathbf{v}-\mathbf{u_e}\|^2\,\mathbf{dv}. \end{cases}$$

On the other hand, the operator (5), modelling collisions between electrons and ions, is a Lorentz operator. It satisfies the conservation of mass and energy

$$\int_{\mathbb{R}^3} C_{e,i}(f_e)(\mathbf{v})\begin{pmatrix}1\\\|\mathbf{v}-\mathbf{u_e}\|^2\end{pmatrix}\mathbf{dv} = 0.$$

Moreover, the equilibrium states for this operator are given by the set of isotropic functions:

$$\mathrm{Ker}(C_{e,i}) = \{f_e \in L^1((1 + \|\mathbf{v}\|^2)\mathbf{dv}), f_e(\mathbf{v}) = \phi(z), z = \|\mathbf{v}-\mathbf{u_e}\|^2\}.$$

Finally, each convex function ψ of f_e is an entropy for $C_{e,i}(f_e)$,

$$\frac{d}{dt}\int_{\mathbb{R}^3} \psi(f_e)\mathbf{dv} \leqslant 0, \quad t \geqslant 0.$$

In addition to these properties, we present a symmetry property. This property may have some importance, in particular in presence of self-consistent magnetic fields. Indeed, any break of symmetry due to an inadequate discretization method could lead to generation of artificial magnetic fields, *via* current source terms.

Proposition 2.1. *If f_e has the following symmetry property with respect to the direction k at time t_0*

$$f_e(t_0,\mathbf{v}) = f_e(t_0,\mathbf{v}^k), \tag{7}$$

with components for

$$\mathbf{v}_i^k = \begin{cases} +\mathbf{v}_i & \text{if } i \neq k,\\ -\mathbf{v}_i & \text{if } i = k. \end{cases}$$

Then, this symmetry property is preserved with respect to time.

3. Numerical scheme for transport

We present a finite volume approximation for the Vlasov–Maxwell system (1) and (2) without collision operators. Indeed, it is crucial to approximate accurately the transport part of the system to asses the collective behavior[1] of the plasma, that occurs typically at a shorter time scale than the collision processes. We introduce a uniform $1D$ space discretization $(x_{i+1/2})_{i \in I}$, $I \subset \mathbb{N}$, of the interval $(0, L_1)$, in the direction denoted by the index 1. The associated space variable is denoted by x_1. We define the control volumes $C_{i,\mathbf{j}} = (x_{i-1/2}, x_{i+1/2}) \times (\mathbf{v}_{\mathbf{j}-1/2}, \mathbf{v}_{\mathbf{j}+1/2})$, the size of a control volume in one direction in space Δx and velocity Δv.

The velocity variable $\mathbf{v} = {}^t(v_1, v_2, v_3)$ is discretized on the grid $\mathbf{v_j} = \mathbf{j} \Delta v = {}^t(v_{j_1}, v_{j_2}, v_{j_3})$ with $\mathbf{j} = {}^t(j_1, j_2, j_3) \in \mathbb{Z}^3$. Moreover we note $\mathbf{v_{j+1/2}} = {}^t(j_1 + 1/2, j_2 + 1/2, j_3 + 1/2) \Delta v$. Finally, the time discretization is defined as $t^n = n \Delta t$, with $n \in \mathbb{N}$.

Let $f_{i,\mathbf{j}}^n$ be an average approximation of the distribution function on the control volume $C_{i,\mathbf{j}}$ at time t^n, that is

$$f_{i,\mathbf{j}}^n \simeq \frac{1}{\Delta x \Delta v^3} \sum_{C_{i,\mathbf{j}}} f(t^n, x, \mathbf{v}) dx \, \mathbf{dv}.$$

Moreover since the discretization is presented in a simple $1D_x$ space geometry, the electromagnetic field has the following structure: $\mathbf{E} = {}^t(E_1(t, x_1), E_2(t, x_1), 0)$, $\mathbf{B} = {}^t(0, 0, B_3(t, x_1))$. Hence we denote by ${}^t(E_{1,i}^n, E_{2,i}^n)$ an approximation of the electric field ${}^t(E_1, E_2)$ where as $B_{3,i}^n$ represents an approximation of the magnetic field B_3 in the control volume $(x_{i-1/2}, x_{i+1/2})$ at time t^n.

3.1. Second order approximation of a one-dimensional kinetic equation

For the sake of simplicity, we focus on the discretization of a $1D$ kinetic transport equation; the extension to higher dimensions is straightforward on a grid. The generic $1D$ scheme is applied in the five phase space directions, without requiring time splitting techniques between transport terms. In this section, the index 1 is dropped both in space and velocity directions, for this simple $1D_x$ geometry.

Let us consider the following equation for $t \geqslant 0$ and $x \in (0, L)$,

$$\frac{\partial f}{\partial t} + v \frac{\partial f}{\partial x} = 0, \tag{8}$$

where the velocity $v > 0$ is given. By symmetry it is possible to recover the case when v is negative. In the following we skip the velocity variable dependency of the distribution function. Using a time explicit Euler scheme and integrating the $1D$ Vlasov equation on a control volume $(x_{i-1/2}, x_{i+1/2})$, it yields

$$f_i^{n+1} = f_i^n - \frac{\Delta t}{\Delta x} \left(\mathcal{F}_{i+1/2}^n - \mathcal{F}_{i-1/2}^n \right), \tag{9}$$

where $\mathcal{F}_{i+1/2}^n$ represents an approximation of the flux $v f(t^n, x_{i+1/2})$ at the interface $x_{i+1/2}$.

The next step consists in the approximation of the fluxes and the reconstruction of the distribution function. With this aim, we approximate the distribution function $f(t^n, x)$ by $f_h(x)$ using a second order accurate approximation of the distribution function on the interval $[x_{i-1/2}, x_{i+1/2})$, with a reconstruction technique by primitive [25]

$$f_h(x) = f_i^n + \epsilon_i^+ \frac{(x - x_i)}{\Delta x} \left(\overline{f}_{i+1}^n - f_i^n \right). \tag{10}$$

We introduce the limiter

$$\epsilon_i^+ = \begin{cases} 0 & \text{if } (\overline{f}_{i+1}^n - f_i^n)(\overline{f}_i^n - f_{i-1}^n) < 0, \\ \min\left(1, \frac{2(\|f^0\|_\infty - f_i^n)}{f_i^n - \overline{f}_{i+1}^n}\right) & \text{if } (\overline{f}_{i+1}^n - f_i^n) < 0 \\ \min\left(1, \frac{2f_i^n}{\overline{f}_{i+1}^n - f_i^n}\right) & \text{else}, \end{cases} \tag{11}$$

and set $\mathcal{F}_{i+1/2}^n = v f_h(x_{i+1/2})$. This type of limiter introduces a particular treatment for extrema. At this price only (dissipation at extrema), we were able to recover correctly the two-stream instability test case, without oscillations destroying the salient features of the distribution function structure. Another choice for the limitation consists in choosing the "Van Leer's one parameter family of the minmod limiters" [31,32]

---

[1] By collective effects, we denote here the self-consistent interaction of electromagnetic fields and particles. Some collective effects are also considered in the collision processes, which make two particles interact *via* the Coulomb field. The self-consistent electrostatic field then screens the long-range Coulomb potential and removes the singularity in the Fokker–Plank–Landau operator.

$$\epsilon_i^+ = \text{minmod}\left(b\,\frac{\overline{f_{i+1}^n} - f_i^n)}{\Delta x}, \frac{\overline{f_{i+1}^n} - f_{i-1}^n)}{2\Delta x}, b\,\frac{\overline{f_i^n} - f_{i-1}^n)}{\Delta x}\right), \tag{12}$$

where

$$\text{minmod}(x, y, z) \equiv \max(0, \min(x, y, z)) + \min(0, \max(x, y, z)), \quad (x, y, z) \in \mathbb{R}^3,$$

and $1 \leqslant b \leqslant 2$. The importance of the choice of limiters will be observed on the two-stream instability test case.

Finally, this reconstruction ensures the conservation of the average and the positivity on $f_h(x)$ [25].

3.2. Fourth order transport scheme

We turn now to a higher order approximation (fourth order MUSCL TVD scheme) [27]. This scheme has also been considered in [28], in the frame of VFRoe schemes for the shallow water equations, where the authors proposed an additional limitation. Here we note that an optimized limitation procedure is possible in our case, breaking the similar treatment for both right and left increments, and taking advantage of the structure of the flux in the non-relativistic Vlasov equation: the force term does not depend of the advection variable.

For this MUSCL scheme, we only give here the algorithm for the implementation of this scheme and refer to [28,27] for the derivation procedure of this scheme.

The high order flux at the interface $x_{i+1/2}$, at time t^n reads

$$\mathcal{F}_{i+1/2}^n = \mathcal{F}\left(f_{i,r}^n, f_{i+1,l}^n\right) = \begin{cases} v f_{i,r}^n & \text{if } v > 0, \\ v f_{i+1,l}^n & \text{if } v < 0. \end{cases}$$

This numerical flux involves the reconstructed states: $f_{i,r}^n = f_i^n + (\Delta f)_i^+$ and $f_{i,l}^n = f_i^n + (\Delta f)_i^-$, where $(\Delta f)_i^\pm$ are the reconstruction increments.

An intermediate state f_i^*, defined by $\frac{1}{3}\left(f_{i,r}^n + f_i^* + f_{i,l}^n\right) = f_i^n$ is introduced. It is shown in [28] that the introduction of this intermediate state preserves, provided the CFL condition is formally divided by three, the positivity of the distribution function. Following [27,28], the fourth order MUSCL reconstruction reads

---

Algorithm of reconstruction.

Compute

$$(\Delta f)_i^- = -\tfrac{1}{6}(2\Delta^* \bar{f}_{i-1/2} + \Delta^* \tilde{f}_{i+1/2}),$$
$$\Delta f)_i^+ = \tfrac{1}{6}(\Delta^* \bar{f}_{i-1/2} + 2\Delta^* \tilde{f}_{i+1/2}),$$

where
$$\Delta^* \bar{f}_{i-1/2} = \text{minmod}(\Delta^* f_{i-1/2}, 4\Delta^* f_{i+1/2}),$$
$$\Delta^* \tilde{f}_{i+1/2} = \text{minmod}(\Delta^* f_{i+1/2}, 4\Delta^* f_{i-1/2})$$

and
$$\Delta^* f_{i+1/2} = \Delta f_{i+1/2} - \tfrac{1}{6}\Delta^3 \bar{f}_{i+1/2},$$
$$\Delta^3 \bar{f}_{i+1/2} = \Delta \bar{f}_{i-1/2}^a - 2\Delta \bar{f}_{i+1/2}^b + \Delta \bar{f}_{i+3/2}^c,$$

with
$$\Delta \bar{f}_{i-1/2}^a = \text{minmod}(\Delta f_{i-1/2}, 2\Delta f_{i+1/2}, 2\Delta f_{i+3/2}),$$
$$\Delta \bar{f}_{i+1/2}^b = \text{minmod}(\Delta f_{i+1/2}, 2\Delta f_{i+3/2}, 2\Delta f_{i-1/2}),$$
$$\Delta \bar{f}_{i+3/2}^c = \text{minmod}(\Delta f_{i+3/2}, 2\Delta f_{i-1/2}, 2\Delta f_{i+1/2}),$$

with the notation $\Delta f_{i+1/2} = f_{i+1} - f_i$.

Reminding that the minmod limiter is given by

$$\text{minmod}(x, y) = \begin{cases} 0 & \text{if } xy \leqslant 0, \\ x & \text{if } |x| \leqslant |y|, \\ y & \text{else}, \end{cases} \tag{13}$$

with $(x, y) \in \mathbb{R}^3$. The limitation proposed in [28] is then applied and allows the positivity of the reconstructed states to be satisfied.

Algorithm for the limitation involving the intermediate state

Compute $(\Delta f)_i^{\lim,\pm}$ such that
$$f_i^n + (\Delta f)_i^{\lim,-} \geq 0,$$
$$f_i^n + (\Delta f)_i^{\lim,+} \geq 0,$$

and
$$f_i^* = f_i^n - (\Delta f)_i^{\lim,-} - (\Delta f)_i^{\lim,+} \geq 0.$$
This limitation reads:
$$\begin{cases} (\Delta f)_i^{\lim,-} = \theta \max\left(\overline{(\Delta f)_i^-}, -f_i^n\right), \\ (\Delta f)_i^{\lim,+} = \theta \max\left(\overline{(\Delta f)_i^+}, -f_i^n\right), \end{cases}$$

where
$$\theta = \begin{cases} 1 & \text{if } \max\left(\overline{(\Delta f)_i^-}, -f_i^n\right) + \max\left(\overline{(\Delta f)_i^+}, -f_i^n\right) \leq 0, \\ \min\left(1, \frac{f_i^n}{\max\left((\Delta f)_i^-, -f_i^n\right) + \max\left((\Delta f)_i^+, -f_i^n\right)}\right) & \text{otherwise.} \end{cases}$$

3.3. Application to the Vlasov–Maxwell system   We exactly follow the same idea to design a scheme for the full Vlasov equation in phase space $(\mathbf{x}, \mathbf{v}) \in \Omega \times \mathbb{R}^3$. In addition, a centered formulation for the electromagnetic fields is chosen:

$$\mathbf{E}^{n+1/2} = \frac{1}{2}(\mathbf{E}^{n+1} + \mathbf{E}^n) \quad \text{and} \quad \mathbf{B}^{n+1/2} = \frac{1}{2}(\mathbf{B}^{n+1} + \mathbf{B}^n). \tag{14}$$

The discretization of the Maxwell equations (2) and (3) is performed *via* an implicit θ-scheme, with $\theta = 1/2$, which corresponds to the Crank–Nicholson scheme and thus preserves the total discrete energy. This discretization is presented in a simple $1D$ space geometry. The electric field $\mathbf{E} = {}^t(E_1, E_2, 0)$ and the magnetic field $\mathbf{B} = {}^t(0, 0, B_3)$ are collocated data on the discrete grid. These fields are solution of the system

$$\begin{cases} \frac{E_{1,i}^{n+1} - E_{1,i}^n}{\Delta t} = -\frac{J_{1,i}^n}{\epsilon_0}, \\ \frac{E_{2,i}^{n+1} - E_{2,i}^n}{\Delta t} + c^2 \frac{B_{3,i+1}^{n+1/2} - B_{3,i-1}^{n+1/2}}{2\Delta x} = -\frac{J_{2,i}^n}{\epsilon_0}, \\ \frac{B_{3,i}^{n+1} - B_{3,i}^n}{\Delta t} + \frac{E_{2,i+1}^{n+1/2} - E_{2,i-1}^{n+1/2}}{2\Delta x} = 0. \end{cases} \tag{15}$$

This scheme is well suited for the situations involving the electromagnetic fields that are treated in the test cases.

The approximation for the current in (15) J_1^n and J_2^n has been chosen such as

$$J_{1,i}^n = \sum_{\mathbf{j} \in \mathbb{Z}^3} \Delta v^3 v_{j_1} f_{i,\mathbf{j}}^n \quad \text{and} \quad J_{2,i}^n = \sum_{\mathbf{j} \in \mathbb{Z}^3} \Delta v^3 v_{j_2} f_{i,\mathbf{j}}^n. \tag{16}$$

Unfortunately, these expressions do not preserve the total energy when slopes limiters are active, but we will show that they have the important feature to reproduce the discrete two-stream dispersion relation.

First, we remind discrete properties concerning positivity, mass and energy conservation [25] of the second order scheme (9) and (10) coupled with (14)–(16), considering now the magnetic component.

Proposition 3.1. *Let the initial datum $(f_{\mathbf{i},\mathbf{j}}^0)_{\mathbf{i},\mathbf{j} \in \mathbb{Z}^3}$ be nonnegative and assume the following CFL type condition on the time step*

$$\Delta t \leq C \min(\Delta x, \Delta v), \tag{17}$$

where $C > 0$ is related to the maximum norm of the electric and magnetic fields and the upper bound of the velocity domain.

Then the scheme (9) and (10) coupled with (14)–(16), when extended to the infinite $3D_{\mathbf{x}} \times 3D_{\mathbf{v}}$ geometry, gives a nonnegative approximation, preserves total mass and energy when slopes limiters are not active on the transport in the velocity directions

$$\frac{1}{2} \sum_{\mathbf{i} \in I} \Delta x^3 \left\{ \epsilon_0 \|\mathbf{E}_{\mathbf{i}}^n\|^2 + \frac{1}{\mu_0} \|\mathbf{B}_{\mathbf{i}}^n\|^2 + m_e \left[\sum_{\mathbf{j} \in \mathbb{Z}^3} \Delta v^3 \|\mathbf{v}_{\mathbf{j}}\|^2 f_{\mathbf{j}}^n \right] \right\} = C^0, \quad n \in \mathbb{N}.$$

Remark 3.2. Both the second order scheme and its fourth order extension preserve the positivity of the distribution function, provided the CFL criteria are satisfied. The positivity is essential to describe correctly the high energy tail of the distribution function, where the particle density is. In all test cases presented, the time increment is chosen small enough to satisfy this CFL condition, together with the diffusive-type CFL condition that comes from the collision operators.

In addition to these properties, we justify our choice for the numerical current thanks to a discrete dispersion relation on the two-stream instability. In the rest of the section, we drop the index 1 on the variables x_1, v_1, E_1 and J_1, because the transport is considered $1D_x \times 1D_v$.

Proposition 3.3. *Consider the second order scheme* (9) *and* (10) *coupled with* (14)–(16) *, when slope limiters are not active, to approximate the Vlasov–Ampère system*

$$\begin{cases} \frac{\partial f}{\partial t} + v \frac{\partial f}{\partial x} + \frac{q_e}{m_e} E \frac{\partial f}{\partial v} = 0, \\ \frac{\partial E}{\partial t} = -\frac{J}{\epsilon_0}. \end{cases} \tag{18}$$

Then the definition (16) *for the current J defines a discrete dispersion relation that converges toward the continuous dispersion relation when* Δv, Δx *and* Δt *tend to* 0.

Proof. The two-stream instability configuration can be fully analyzed with the Vlasov–Ampère system (18) extracted from Eqs. (1)–(3). The dispersion relation for a perturbation $f^{(1)} \propto e^{i(kx-\omega t)}$ of an initial equilibrium state $f^{(0)}$, with $\|f^{(1)}\| \ll \|f^{(0)}\|$, then reads

$$1 + \frac{q_e^2}{\epsilon_0 m_e} \sum_{\mathbb{R}} \frac{v}{\omega(\omega - kv)} \frac{\partial f^{(0)}}{\partial v} dv = 0. \tag{19}$$

Here the crucial point is the discretization on the velocity part of the phase space, so that we perform a semi-discrete analysis. In the frame of the discretization (9) and (10) coupled with (14)–(16), we consider the semi-discrete scheme approximating (18)

$$\begin{cases} \frac{\partial f}{\partial t} + v \frac{\partial f}{\partial x} + \frac{q_e}{m_e} E \frac{f_{j+1/2} - f_{j+1/2}}{\Delta v} = 0, \\ \frac{\partial E}{\partial t} = -\frac{q_e}{\epsilon_0} \sum_{j \in \mathbb{Z}} \Delta v v_j f_j, \end{cases} \tag{20}$$

with

$$f_{j+1/2} = \frac{f_{j+1} + f_j}{2},$$

assuming the slope limiter is not active. Then we perform a discrete linearization around an equilibrium state

$$f_j = f_j^{(0)} + f_j^{(1)},$$

where $\|f^{(1)}\| \ll \|f^{(0)}\|$. Using $f_j^{(1)} \propto e^{i(kx-\omega t)}$ in (20), it yields

$$\begin{cases} -i(\omega - kv_j) f_j^{(1)} + \frac{q_e}{m_e} E^{(1)} \frac{f_{j+1/2}^{(0)} - f_{j-1/2}^{(0)}}{\Delta v} = 0, \\ -i\omega E^{(1)} = -\frac{q_e}{\epsilon_0} \sum_{j \in \mathbb{Z}} \Delta v v_j f_j^{(1)}. \end{cases} \tag{21}$$

These equations lead to the discrete dispersion relation

$$1 + \frac{q_e^2}{\epsilon_0 m_e} \sum_{j \in \mathbb{Z}} \frac{v_j}{\omega(\omega - kv_j)} \left[\frac{f_{j+1/2}^{(0)} - f_{j-1/2}^{(0)}}{\Delta v} \right] \Delta v = 0. \tag{22}$$

We recover the continuous dispersion relation (19) when passing to the limit $\Delta v \to 0$. Any other choice for the discrete current in (21) would introduce an additional error of order $O(\Delta v^2)$ in the dispersion relation (22). For instance, the choice

$$J = \sum_{j \in \mathbb{Z}} \Delta v v_j f_{j+1/2}$$

would lead to the

$$1 + \frac{q_e^2}{\epsilon_0 m_e} \sum_{j \in \mathbb{Z}} \frac{(v_j - \Delta v)}{\omega(\omega - kv_j)} \left[\frac{f_{j+1/2}^{(0)} - f_{j-1/2}^{(0)}}{\Delta v} \right] \Delta v = 0, \tag{23}$$

which is a "shifted" dispersion relation, with a $O(\Delta v)$ accuracy, compared to the second order accurate relation given by (22). □

3.4. Boundary conditions

3.4.1. Truncation of the velocity domain

The discretization in the velocity space imposes a truncation of the infinite velocity domain, and the introduction of boundary conditions. We only need to consider the direction v_1, where the discretized velocity variable is v_{j_1}, with $j_1 \in [-n_{v_1}, n_{v_1}] \subset \mathbb{Z}$, and $2n_{v_1} + 1$ is the total number of discretization points. If the second order scheme (respectively the fourth order scheme) is considered, then the boundary conditions are applied on two ghost points (respectively three ghost points). This is due to the extension of the stencil. Considering the second order scheme, the ghost points at the velocity domain are v_{j_1} with $j_1 = \pm n_{v_1}, \pm(n_{v_1} + 1)$. Therefore, at these points, we impose the truncation $f_{j_1}^{n+1} = 0$.

3.4.2. Boundary conditions in the space domain

The boundary conditions for the space directions satisfy also naturally the positivity constraint with our scheme. It is indeed designed with reconstructed numerical fluxes, that maintain the positivity (under the CFL condition) if the distribution function at the previous time step is positive. At a boundary interface, $x_{-1/2}$ at the left boundary, where the numerical flux should be computed, the only requirement is to specify a positive distribution at ghost points to impose the boundary conditions. We explicit here the non-trivial ghost point used by a zero current left boundary (with temperature T_L) condition, in the direction x_1:

$$f_{-1,\mathbf{j}}^n = C_{-1/2} \exp\left(-\frac{\|v_{\mathbf{j}}\|^2}{2T_L}\right),$$

(24)

where $C_{-1/2} > 0$ and satisfies

$$\sum_{\mathbf{j}} \mathcal{F}_{-1/2,\mathbf{j}}^n = 0.$$

(25)

4. Numerical simulations in the collisionless regime

We first propose a validation strategy in the linear, collisionless regime, based on the work of Sartori and Coppa [33], to describe the transient behavior of the solution to the Vlasov–Poisson system, in the non-relativistic and relativistic cases, when the initial data are close to the equilibrium. Their approach, relying on Green kernels, is recalled in Appendix A, in the non-relativistic regime. Our aim is to capture kinetic effects in the linear regime, such as the Landau damping and the two-stream instability. A semi-analytical solution is obtained, with a prescribed accuracy. Moreover, this method allows the exploration of wavenumber ranges, where other approaches relying on dispersion relations fail. We recall that classical validations of kinetic solvers dedicated to plasma physics [25,34] are based on the calculation of the growth rates (instability), or decrease rates (damping) in the linear regime. We will show the efficiency of the semi-analytical method on the two-stream instability test case.

The transport schemes are tested, without collision operators, with a low number of dimensions, $1D_x \times 1D_v$ for the test 1 (the computational resources are then very low), or $1D_x \times 3D_v$ for the test 2. For this latter test, a parallelisation technique is employed, with a domain decomposition in the space dimension. The simulation is performed with 42 processors to accelerate the calculations, on the CEA-CCRT-platine facility. This facility is a cluster of Novascale 3045 servers, including 932 nodes, each one having 4 Intel Itanium dual core processors, at 1.6 GHz. Each processor has a memory of 24 Go. The Novascale servers are interconnected by a Voltaire network, with technology Infiniband DDR. We first present the appropriate scaling to be considered.

4.1. Scaling with the plasma frequency

Scaling parameters can be introduced to obtain a dimensionless form of the Vlasov–Maxwell–Fokker–Planck equations. The plasma frequency ω_{pe}, the Debye length λ_D, the thermal velocity of electrons v_{th}, and the cyclotron frequency ω_{ce} are defined as follows

$$\omega_{pe} = \sqrt{\frac{n_0 e^2}{\epsilon_0 m_e}}, \quad \lambda_D = \sqrt{\frac{\epsilon_0 \kappa_B T_0}{n_0 e^2}}, \quad v_{th} = \sqrt{\frac{\kappa_B T_0}{m_e}}, \quad \omega_{ce} = \frac{eB}{m_e}.$$

(26)

These parameters enable us to define dimensionless parameters marked with tilde:

- Dimensionless time, space and velocity, respectively,

$$\tilde{t} = \omega_{pe} t, \quad \tilde{x} = \frac{x}{\lambda_D}, \quad \tilde{v} = \frac{v}{v_{th}}.$$

(27)

- Dimensionless electric field, magnetic field and distribution function, respectively,

$$E = \frac{eE}{m_e v_{th} \omega_{pe}}, \quad B = \frac{eB}{m_e \omega_{pe}} = \frac{\omega_{ce}}{\omega_{pe}}, \quad \tilde{f}_e = f_e \frac{v_{th}^3}{n_0}. \tag{28}$$

This leads to the following dimensionless equations

$$\begin{cases} \frac{\partial f_e}{\partial t} + \nabla_{\mathbf{x}} \cdot (\mathbf{v} f_e) - \nabla_{\mathbf{v}} \cdot ((\mathbf{E} + \mathbf{v} \times \mathbf{B}) f_e) = \frac{v}{Z} C_{e,e}(f_e, f_e) + v C_{e,i}(f_e), \\ \frac{\partial \mathbf{E}}{\partial t} - \frac{1}{\beta^2} \nabla_{\mathbf{x}} \times \mathbf{B} = n\mathbf{u}, \\ \frac{\partial \mathbf{B}}{\partial t} + \nabla_{\mathbf{x}} \times \mathbf{E} = 0, \\ \nabla_{\mathbf{x}} \cdot \mathbf{E} = (1 - n), \quad \nabla_{\mathbf{x}} \cdot \mathbf{B} = 0, \end{cases} \tag{29}$$

where $\beta = v_{th}/c$, v is the ratio between electron–ion collision frequency and plasma frequency

$$v = \frac{Zn_0 e^4 \ln \Lambda}{8\pi\epsilon_0^2 m_e^2 v_{th}^3 \omega_{pe}} = \frac{Z \ln \Lambda}{8\pi n_0 \lambda_D^3} = \frac{v_{e,i}}{\omega_{pe}} \quad \text{with } v_{e,i} = \frac{Zn_0 e^4 \ln \Lambda}{8\pi\epsilon_0^2 m_e^2 v_{th}^3}.$$

The zero and first order moments of the distribution function are

$$\begin{cases} n(t, \mathbf{x}) = \int_{\mathbb{R}^3} f_e(t, \mathbf{x}, \mathbf{v}) d\mathbf{v}, \\ \mathbf{u}(t, \mathbf{x}) = \frac{1}{n(t, \mathbf{x})} \int_{\mathbb{R}^3} f_e(t, \mathbf{x}, \mathbf{v}) \mathbf{v} \, d\mathbf{v}, \end{cases}$$

which are normalized respectively by n_0 and v_{th}.

Moreover, in (29) the dimensionless collision operators are considered

$$\begin{cases} C_{e,e}(f_e, f_e) = \nabla_{\mathbf{v}} \cdot \overleftarrow{\int_{\mathbb{R}^3}} \Phi(\mathbf{v} - \mathbf{v}')[f_e(\mathbf{v}')\nabla_{\mathbf{v}} f_e(\mathbf{v}) - f_e(\mathbf{v})\nabla'_{\mathbf{v}} f_e(\mathbf{v}')] d\mathbf{v}'), \\ C_{e,i}(f_e) = \nabla_{\mathbf{v}} \cdot [\Phi(\mathbf{v})\nabla_{\mathbf{v}} f_e(\mathbf{v})], \end{cases} \tag{30}$$

with Φ given by (6).

4.2. Test 1: 1D two-stream instability

The ICF physics involves a propagation of electron beams in plasma. The plasma response to the beam consists in a return current that goes in the opposite direction to the beam in order to preserve the quasineutrality. This leads to a very unstable configuration favorable to the excitation of plasma waves. We focus here on the instability with a perturbation wavevector parallel to the beam propagation direction, namely the two-stream instability. Of course, this stands as an academic numerical test but it is closely related to the physics of ICF.

This numerical test is a very demanding for numerical schemes of transport, that have to be specially designed (see Proposition 3.3). In particular, a discrete dispersion relation relative to that problem is developed to justify numerical choices for the second order scheme. For this scheme also, during the limitation procedure, an additional dissipation at extrema is introduced, compared to [25], in order to preserve the solution from spurious oscillations. We will show the sensitivity of the scheme with respect to the chosen limiter, for this particular test case. Moreover, the fourth order scheme is introduced to reduce numerical heating, for simulations intended to deal with the two-stream instability.

We consider the $1D_x \times 1D_v$ Vlasov–Ampère system (18) and choose the scaling (26)–(28), with $v = 0$. The initial distribution function and electric field are

$$\begin{cases} f^0(x, v) = \frac{1}{2}[(1 + A\cos(kx))\mathcal{M}_{1,v_d}(v) + (1 - A\cos(kx))\mathcal{M}_{1,-v_d}(v)], \\ E^0(x) = 0, \end{cases}$$

where

$$\mathcal{M}_{1,v_d}(v) = \frac{1}{\sqrt{2\pi}} \exp\left(-\frac{\|v - v_d\|^2}{2}\right)$$

is the Maxwellian distribution function centered around v_d.

In order to compare the numerical dissipation associated to the second and fourth order schemes, we choose a strong perturbation amplitude $A = 0.1$. The perturbation wavelength is $k = 2\pi/L$ and the beam initial mean velocities are $v_d = \pm 4$, $L = 25$ being the size of the periodic space domain. We choose a truncation of the velocity space to be $v_{max} = 12$ and time steps are chosen to be $\Delta t = 1/200$, such as to satisfy the CFL criteria and maintain the positivity of the distribution function.

The objectives of this numerical simulation are on the one hand to compare the second order finite volume scheme (specially designed to conserve exactly the discrete total energy, except if the slope limiters are active) for different slope limiters and the fourth order MUSCL scheme. On the other hand we want to explore the effect of a reduced number of grid points on the conservation of the discrete invariants.

In Fig. 1, two countersteaming beams that are initially well separated in the phase space (a) start to mix together. They finally create a complicated vortex structure, involving wave–particle interactions. This behavior remains quantitatively the same whatever the transport scheme is, second or fourth order. In Fig. 2, we present the evolution of the electric energy for different schemes and several configurations from 32^2 points to 256^2. We observe that with a reduced number of grid points (smaller than 128 points in velocity), the second order scheme with the slope limiters (11), and fourth order scheme, present a different behavior on the total electric energy and total energy. Indeed, for a reduced grid resolutions (32^2 or 64^2 points), the fourth order scheme proves to be better than the second order one. For 32^2 points, plasma oscillations at the plasma frequency in the nonlinear phase are not reproduced with the second order scheme, whereas they can be seen with the fourth order scheme (see Fig. 2). Moreover for this resolution, the transition from the linear phase to the nonlinear phase occurs earlier than it should for the second order scheme. Furthermore, as the grid resolution increases, the accuracy remains better for the fourth order scheme than for the second order one in the nonlinear phase. The convergence toward curves with 128^2 or 256^2 resolution grid is indeed better. We recall that quantities in Fig. 2 are plotted with a logarithmic scale, that smoothes out discrepancies between curves. In addition to these results, the respect of total discrete energy conservation proves to be better for the fourth order scheme than for the second order one at a reduced grid resolution, see Figs. 3 and 4.

The use of the slope limiters (12) for the second order scheme improves the results. The plasma wave structure can then be captured at reduced grid resolutions, see Fig. 2(b) and (c). However, the energy dissipation remains quantitatively the same as the second order scheme with the limiters (11), see Figs. 3 and 4. Only in the case of the second order scheme without limiter, could the energy be exactly conserved. The counterpart would be the loss of any exploitable solution (loss of stability).

As this test case requires both a good preservation of invariants and accuracy when nonlinear phenomena occur, we might conclude that the fourth order scheme, with a resolution along each velocity direction greater than 32 cells, is well suited for our physical applications.
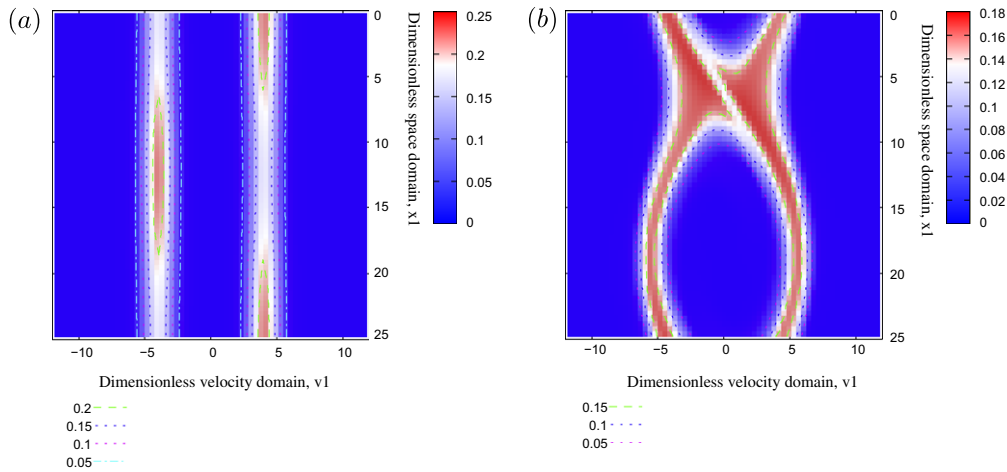

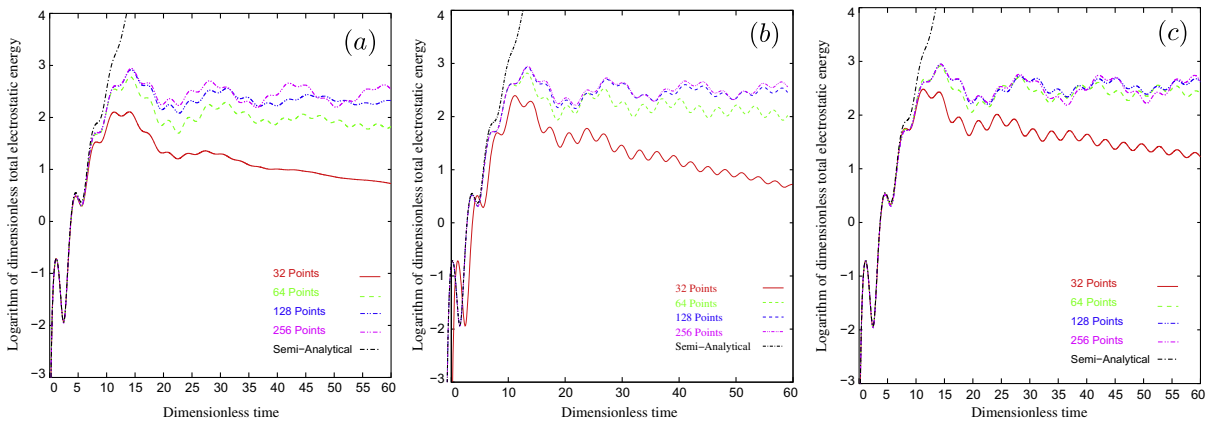**Fig. 1.** Beams phase space (a) at initial time and (b) at 20 plasma periods (after saturation), with 64^2 grid points.

Fig. 2. Evolution of the electrostatic energy for 32^2, 64^2, 128^2, 256^2 grid points, and the semi-analytical solution in the linear regime. Results are shown for the second order with (a) slope limiters (11) and (b) slope limiters (12) with $b = 2$ and (c) fourth order transport scheme.
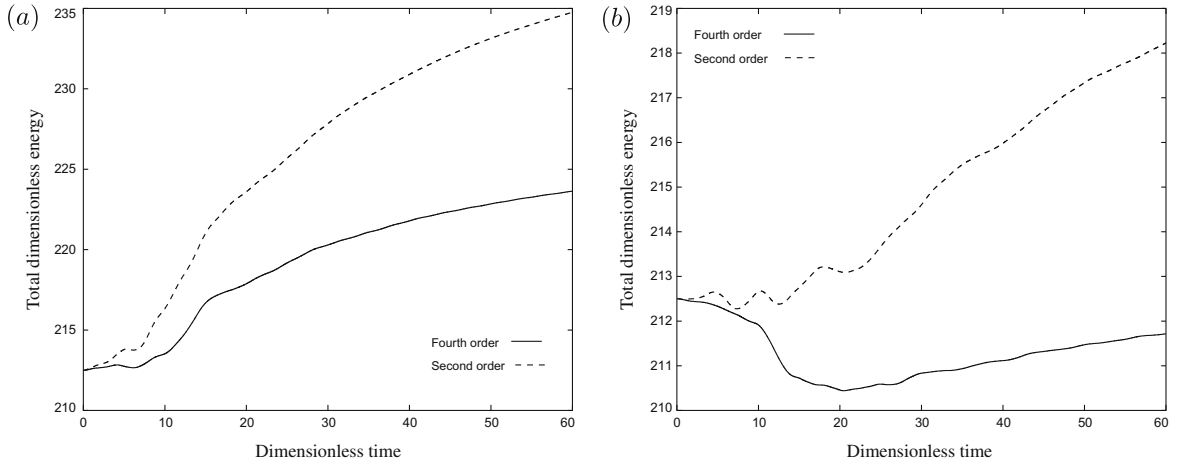
Fig. 3. Comparison of the energy evolution for the second (with limiter (11)) and fourth order transport schemes. Results are shown (a) for 32^2 and (b) 64^2 grid points.
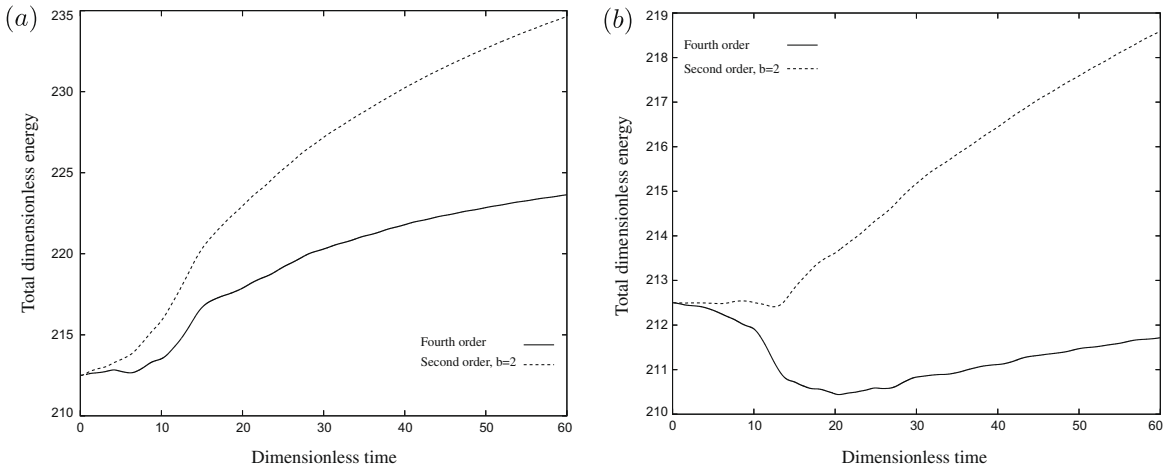

Fig. 4. Comparison of the energy evolution for the second (with limiter (12), $b = 2$) and fourth order transport schemes. Results are shown (a) for 32^2 and (b) 64^2 grid points.

4.3. Test 2: 1D X-mode plasma in a magnetic field

This numerical test stands as a validation of the schemes in the linear regime when the Vlasov equation is coupled with the Maxwell system, without the collisions between particles. The second order scheme is used for the transport terms in the x_1, v_1, v_2 and v_3 directions. A particular initial data is chosen (see the derivation in Appendix B) to trigger an X-mode plasma wave at a well-defined frequency ω. This type of wave presents a mixed polarization (longitudinal and transverse with respect to the magnetic field), that propagates in the plane $P_\perp$, perpendicular to the magnetic field direction.

The chosen frequency ω is a solution of the dispersion relation (74) of the linearized Vlasov–Maxwell equations, introducing the equilibrium state $f^{(0)}(\|\mathbf{v}\|^2)$. The initial data are chosen such that $f^{(0)}$, E_1, E_2 and B_3 only depend on ω, $B^{(0)}$, $k_1 = 2\pi/L_1$ and A; where $\hat{f}_n$, B_3, E_1 and E_2 are the reconstructed (in Appendix B) Fourier transforms of the distribution function and electromagnetic fields. The magnetic field $B^{(0)}$ is the nonperturbed magnitude of the magnetic field, L_1 is the length of the periodic space domain, A is the perturbation amplitude. The initial data can then be constructed with the help of truncated Fourier series

$$
\begin{cases}
f^{(0)}(x_1, \mathbf{v}) = f^{(0)}(\|\mathbf{v}\|^2) + \sum_{n=-2}^{2} \hat{f}_n(\mathbf{v}_\perp) e^{ik_1 x_1 + in\psi}, & x_1 \in (0, L_1),\ \mathbf{v} \in \mathbb{R}^3, \\
E_1(t, x_1) = E_1 e^{-i\omega t + ik_1 x_1}, & x_1 \in (0, L_1), \\
E_2(t, x_1) = E_2 e^{-i\omega t + ik_1 x_1}, & x_1 \in (0, L_1), \\
B(t, x_1) = B^{(0)} + B_3 e^{-i\omega t + ik_1 x_1}, & x_1 \in (0, L_1).
\end{cases}
$$

We define ψ as the angle in the cylindrical coordinates for the velocity, where the axial direction is the magnetic field direction (see Appendix B).

The scaling is defined by the relations (26)–(28), with $v = 0$. We choose $B^{(0)} = 2$ and a rather strong amplitude perturbation $A = 0.1$ with periodic boundary conditions on the space domain and $\beta = v_{th}/c = 0.05$. Hence, the dispersion relation has been solved for these parameters. One of the solution $\omega \simeq 5.1432$ is choosen in the initial data set.

We considered 126 points along the 1D space direction, and 64 points along each velocity direction $\mathbf{v} = {}^t(v_1, v_2, v_3)$. The dimension of the space domain is $L_1 = 25$, whereas the truncation of the velocity space occurs at $v_{max} = 7$ for each velocity direction. Furthermore, the time step is $\Delta t = 1/200$, which ensures the positivity of the distribution function here.

The Fourier spectrum in Fig. 5(a) exhibits a well defined frequency $f = 1/T \simeq 1.6375$ (corresponding to a period T) for the total magnetic energy, that corresponds to a frequency $f/2$ for the magnetic field oscillations. We finally find $\omega = 2\pi f/2 \simeq 5.1443$ from the numerical solution, to be compared with the analytical results 5.1432. This proves a good accuracy of the numerical results, while the distribution function is greatly affected by the magnetic field. As an illustration, we show in Fig. 5(c) how the magnetic field makes the distribution function rotate in the velocity space perpendicular to the magnetic field axis.

5. Approximation of the collision operators

In this section, we focus on the approximation of collision operators. Since the space variable is a parameter, we only consider the space homogeneous equation,

$$\begin{cases} \frac{\partial f}{\partial t} = C_{e,e}(f,f) + C_{e,i}(f), \\ f(0, \mathbf{v}) = f^{(0)}(\mathbf{v}), \end{cases}$$

where $C_{e,e}(f,f)$ and $C_{e,i}(f)$ are given by (30).

5.1. Discretization of the Lorentz operator

We consider $f_\mathbf{j}$ an approximation of the distribution function $f(\mathbf{v_j})$ and introduce the operator $\mathbf{D}$, which denotes a discrete form of the usual gradient operator $\nabla_\mathbf{v}$, whereas $\mathbf{D}^*$ represents its formal adjoint, which represents an approximation of $-\nabla_\mathbf{v}$. Therefore, for any test sequence $(\psi_\mathbf{j})_{\mathbf{j} \in \mathbb{Z}^3}$, we set $(\mathbf{D}\psi_\mathbf{j})_{\mathbf{j} \in \mathbb{Z}^3}$ as a sequence of vectors of $\mathbb{R}^3$

$$\mathbf{D}\psi_\mathbf{j} = {}^t(D_1\psi_\mathbf{j}, D_2\psi_\mathbf{j}, D_3\psi_\mathbf{j}) \in \mathbb{R}^3,$$

where D_s is an approximation of the partial derivative $\frac{\partial}{\partial v_s}$ with $s \in \{1, 2, 3\}$. In order to preserve the property of decreasing entropy at the discrete level, we use the log weak formulation of the Lorentz operator [17]

$$\sum_{\mathbb{R}^3} C_{e,i}(f)(\mathbf{v})\psi(\mathbf{v})\mathbf{dv} = -\sum_{\mathbb{R}^3} \Phi(\mathbf{v})f(\mathbf{v})\nabla_\mathbf{v} \log(f(\mathbf{v})) \cdot \nabla_\mathbf{v}\psi(\mathbf{v})\mathbf{dv},$$

where Φ is given by (6) and ψ is a smooth test function. Then, using the notations previously introduced, the discrete operator $C_{e,i}^{\Delta v}(f)$ is given by
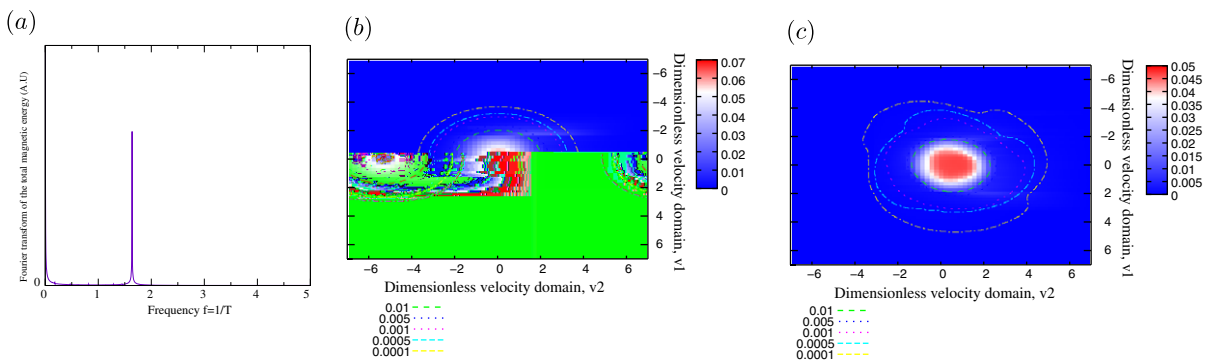

Fig. 5. Discrete Fourier spectrum in frequency (a) of the discrete analogous of the total dimensionless magnetic energy $\int_0^{L_1} \frac{\|B_1\|^2}{2} dx_1$. Projection on the $v_1 - v_2$ velocity domain for the distribution function is shown at initial time $t_n = 0$ (b) and at $t_n = 40$ (c), for a particular point of the space domain, $x_1 = 0$, $v_3 = 0$.

$$C_{e,i}^{\Delta v}(f)(\mathbf{v_j}) = -\mathbf{D}^*\left[\frac{1}{\|\mathbf{v_j}\|^3}S(\tilde{\mathbf{v}}_\mathbf{j})f_\mathbf{j}\mathbf{D}(\log(f_\mathbf{j}))\right], \tag{31}$$

where $S(\tilde{\mathbf{v}}_\mathbf{j})$ is the following matrix

$$S(\tilde{\mathbf{v}}_\mathbf{j}) = \|\tilde{\mathbf{v}}_\mathbf{j}\|^2\mathrm{Id} - \tilde{\mathbf{v}}_\mathbf{j}\otimes\tilde{\mathbf{v}}_\mathbf{j}.$$

Now, $\tilde{\mathbf{v}}_\mathbf{j}$ has to satisfy the discrete conservation of energy

$$\frac{D_1(\|\mathbf{v_j}\|^2)}{\tilde{\mathbf{v}}_{j_1}} = \frac{D_2(\|\mathbf{v_j}\|^2)}{\tilde{\mathbf{v}}_{j_2}} = \frac{D_3(\|\mathbf{v_j}\|^2)}{\tilde{\mathbf{v}}_{j_3}}. \tag{32}$$

Then, we consider the 8 uncentered operators $\mathbf{D}^\epsilon$, with the formalism:

$$\mathbf{D}^\epsilon = {}^t(D_1^{\epsilon_1}, D_2^{\epsilon_2}, D_3^{\epsilon_3}),$$

with $\epsilon = {}^t(\epsilon_1, \epsilon_2, \epsilon_3)$, and $\epsilon_i \in \{+1, -1\}$ for $i \in \{1, 2, 3\}$. More precisely, the operator D^{ϵ_i} is the forward uncentered discrete operator if $\epsilon_i = +1$ and the backward uncentered discrete operator if $\epsilon_i = -1$:

$$\mathbf{D}^\epsilon\Psi_\mathbf{j} = \frac{1}{\Delta v}\begin{pmatrix} \epsilon_1[\Psi_{j_1+\epsilon_1} - \Psi_{j_1}] \\ \epsilon_2[\Psi_{j_2+\epsilon_2} - \Psi_{j_2}] \\ \epsilon_3[\Psi_{j_3+\epsilon_3} - \Psi_{j_3}] \end{pmatrix}. \tag{33}$$

This 8 operators respectively match to 8 expressions of $\tilde{\mathbf{v}}_\mathbf{j}^\epsilon$, following (32)

$$\tilde{\mathbf{v}}_\mathbf{j}^\epsilon = \frac{1}{2}(\mathbf{v_j} + \mathbf{v_{j+\epsilon}}).$$

This choice has been made to avoid the use of the centered discrete operator that conserves non physical quantities. On the other hand, the uncentered operators, taken separately, introduce some artificial asymmetry in the distribution function leading to a loss of accuracy when coupling to Maxwell equations. To overcome these difficulties, following the idea of [18], we introduce a symmetrization of the discrete operator based on the averaging over the eight uncentered discretizations:

$$C_{e,i}^{\Delta v}(f)(\mathbf{v_j}) = \frac{1}{8}\sum_\epsilon C_{e,i}^\epsilon(f),$$

$$C_{e,i}^\epsilon(f) = -\mathbf{D}^{*,\epsilon}\left[\frac{1}{\|\mathbf{v_j}\|^3}S(\tilde{\mathbf{v}}_\mathbf{j}^\epsilon)f_\mathbf{j}\mathbf{D}^\epsilon(\log(f_\mathbf{j}))\right].$$

This final expression presents the desirable properties: the mass and energy conservation, the entropy decreasing behavior, the positivity preservation of the distribution function in a finite time sequence. The proofs are not detailed here but can be deduced easily from those presented in [25]. Also, it introduces an additional discrete symmetry property, compared to the operator presented in [25]. Indeed, we obtain the operator as an average over the full set of the uncentered operators. The motivation of this averaging comes from the isotropization effect of the Lorentz operator: it diffuses in angle. This averaging leads to a discrete analogous of the symmetry property presented in Proposition 2.1. This symmetry concerns the directions that are aligned with the grid. The symmetries along directions that are not aligned with the grid are preserved with marginal errors.

Proposition 5.1. *Under the condition (32) on $\tilde{\mathbf{v}}_\mathbf{j}$, the discretization (34) to the Lorentz operator (5) satisfies the following properties,*

- *it preserves the mass and energy,*
- *it decreases the discrete entropy*

$$H(t) = \Delta v^3 \sum_{\mathbf{j}\in\mathbb{Z}^3} f_\mathbf{j}(t)\log(f_\mathbf{j}(t)),$$

- *there exists a time-sequence Δt_n such that the scheme*

$$f_\mathbf{j}^{n+1} = f_\mathbf{j}^n + \Delta t C_{e,i}^{\Delta v}(f)(\mathbf{v_j}),$$

defines a positive solution at any time i.e. $\sum_n \Delta t_n = +\infty$.

Furthermore, if $f_\mathbf{j}$ is symmetric with respect to 0 in the direction j_k at time t^n, then this property is preserved at time t^{n+1},

$$\sum_{\mathbf{j}\in\mathbb{Z}^3} C_{e,i}^{\Delta v}(f)(\mathbf{v_j})v_{j_k}\Delta v^3 = 0. \tag{34}$$

Proof. The proofs of all the properties but the last one can be found in [25]. We prove the last property and rewrite the operator (34) in a different manner, assuming we have a symmetry along the velocity direction v_{j_k}

$$C_{e,i}^{\Delta v}(f)(\mathbf{v_j}) = \frac{1}{8} \sum_\epsilon C_{e,i}^\epsilon(f)(\mathbf{v_j}) = \frac{1}{8} \sum_\epsilon \left[\frac{1}{3} \sum_{k=1}^3 \frac{1}{2} \left(C_{e,i}^{\epsilon^{+,(k)}}(\mathbf{v_j}) + C_{e,i}^{\epsilon^{-,(k)}}(\mathbf{v_j}) \right) \right], \tag{35}$$

where the notation $\epsilon^{\pm,(k)}$ refers to

$$\begin{cases} \epsilon_i^{\pm,(k)} = \pm 1 & \text{if } i = k, \\ \epsilon_i^{\pm,(k)} = \epsilon_i & \text{if } i \neq k. \end{cases} \tag{36}$$

We are interested in the cancellation of the operator $\sum_{\mathbf{j} \in \mathbb{Z}^3} C_{e,i}^{\Delta v}(f)(\mathbf{v_j}) v_{j_k}$. This is equivalent to the cancellation of

$$Q^{(k)} := \sum_{\mathbf{j} \in \mathbb{Z}^3} \left(C_{e,i}^{\epsilon^{+,(k)}}(\mathbf{v_j}) + C_{e,i}^{\epsilon^{-,(k)}}(\mathbf{v_j}) \right) v_{j_k}$$

$$= \sum_{\mathbf{j} \in \mathbb{Z}^3} \frac{1}{\|\mathbf{v_j}\|^3} f_{\mathbf{j}} \, S\left(\tilde{\mathbf{v}}_{\mathbf{j}}^{\epsilon^{+,(k)}} \right) \mathbf{D}^{\epsilon^{+,(k)}} \log(f_{\mathbf{j}}) \cdot \mathbf{D}^{\epsilon^{+,(k)}} v_{j_k} + \sum_{\mathbf{j} \in \mathbb{Z}^3} \frac{1}{\|\mathbf{v_j}\|^3} f_{\mathbf{j}} \, S\left(\tilde{\mathbf{v}}_{\mathbf{j}}^{\epsilon^{-,(k)}} \right) \mathbf{D}^{\epsilon^{-,(k)}} \log(f_{\mathbf{j}}) \cdot \mathbf{D}^{\epsilon^{-,(k)}} v_{j_k}.$$

Then, since $\mathbf{D}^{\epsilon^{+,(k)}} v_{j_k} = \mathbf{D}^{\epsilon^{-,(k)}} v_{j_k} = \mathbf{e_k}$, it yields

$$Q^{(k)} = \sum_{\mathbf{j} \in \mathbb{Z}^3} \frac{1}{\|\mathbf{v_j}\|^3} f_{\mathbf{j}} \left(\sum_{i \neq k} \left(\tilde{v}_{j_i}^{\epsilon_i^{+,(k)}} \right)^2 \right) D_k^{\epsilon^{+,(k)}}(\log(f_{\mathbf{j}})) - \sum_{\mathbf{j} \in \mathbb{Z}^3} \frac{1}{\|\mathbf{v_j}\|^3} f_{\mathbf{j}} \tilde{v}_{j_k}^{\epsilon_k^{+,(k)}} \left(\sum_{i \neq k} \tilde{v}_{j_i}^{\epsilon_i^{+,(k)}} D_i^{\epsilon^{+,(k)}}(\log f_{\mathbf{j}}) \right)$$

$$- \sum_{\mathbf{j} \in \mathbb{Z}^3} \frac{1}{\|\mathbf{v_j}\|^3} f_{\mathbf{j}} \left(\sum_{i \neq k} \left(\tilde{v}_{j_i}^{\epsilon_i^{-,(k)}} \right)^2 \right) D_k^{\epsilon^{-,(k)}}(\log(f_{\mathbf{j}})) - \sum_{\mathbf{j} \in \mathbb{Z}^3} \frac{1}{\|\mathbf{v_j}\|^3} f_{\mathbf{j}} \tilde{v}_{j_k}^{\epsilon_k^{-,(k)}} \left(\sum_{i \neq k} \tilde{v}_{j_i}^{\epsilon_i^{-,(k)}} D_i^{\epsilon^{-,(k)}}(\log f_{\mathbf{j}}) \right).$$

Then using definition (36) and the symmetry of $f_{\mathbf{j}}^n$ with respect to 0 in the velocity direction v_{j_k}, we obtain $Q^{(k)} = 0$. Then multiplying (35) by v_{j_k} and integrating in the full velocity space gives the relation (34). This relation implies that $f_{\mathbf{j}}^{n+1}$ is symmetric with respect to 0 in the direction v_{j_k}. □

5.2. Discrete Landau operator

We consider the discretization of the FPL operator (4) on the whole 3D velocity space. It is based on the entropy conservative discretization introduced in [17], where a discrete weak log form of the FPL operator is used. This discretization yields:

$$\begin{cases} \frac{df_{\mathbf{j}}(t)}{dt} = (\mathbf{D}^* \rho(t))_{\mathbf{j}}, & \mathbf{j} \in \mathbb{Z}^3, \\ \rho(t) = \Delta v^3 \sum_{\mathbf{m} \in \mathbb{Z}^3} f_{\mathbf{j}}(t) f_{\mathbf{m}}(t) \Phi(\mathbf{v_j} - \mathbf{v_m})(\mathbf{D}(\log(f(t))_{\mathbf{j}}) - \mathbf{D}(\log f(t))_{\mathbf{m}}), \end{cases} \tag{37}$$

where $\mathbf{D}$ stands for a downwind or upwind finite discrete operator approximating the usual gradient operator $\nabla_{\mathbf{v}}$. This uncentered approximation ensures that the only equilibrium states are the discrete Maxwellian. The use of centered discrete operators would have lead to non physical conserved quantities. The discretization of the FPL operator is then obtained as the average over uncentered operators, but here for a different reason compared to the previous section, on the electron–ion collision operator discretization. In [19], the scheme is rewritten as the sum of two terms: a second order approximation and an artificial viscosity term in Δv^2 which kills spurious oscillations. However, the computational cost of a direct approximation of (37) remains too high. Therefore, a multigrid technique has been used. We refer to [19,35] for the details of the implementation on the FPL operator. Nevertheless, these latter approaches introduce a new approximation than can affect the accuracy. Based on [20], Crouseilles and Filbet proposed another approach and noticed that the discrete FPL operator (37) in the Fourier space can be written as a discrete convolution, which directly gives a fast algorithm. Here we adopt the multigrid method, detailed in [19], that has a complexity of order $O(n_v^3 \log n_v^3)$.

This discrete approximation preserves positivity, mass, momentum, energy, and ensures that the entropy is decreasing. Moreover, the discrete equilibrium states are the discrete Maxwellian. We refer to [17] for the proofs and to [25] for numerical tests cases illustrating these properties in the homogeneous case.

6. Numerical results for the full kinetic model

6.1. Scaling with the collision frequency

For the analysis of collisional processes, a new scaling is introduced here, that allows time steps to be of the order of the electron–ion collision time. In order to take into account transport phenomena occurring at the collision time scale, several parameters are required: the electron–ion collision frequency $\nu_{e,i}$, the associated mean free path $\lambda_{e,i}$, the thermal velocity v_{th} and the cyclotron frequency ω_{ce}

$$v_{e,i} = \frac{Zn_0 e^4 \ln \Lambda}{8\pi\epsilon_0^2 m_e^2 v_{th}^3}, \quad \lambda_{e,i} = \frac{v_{th}}{v_{e,i}}, \quad v_{th} = \sqrt{\frac{\kappa_B T_0}{m_e}}, \quad \omega_{ce} = \frac{eB}{m_e}. \tag{38}$$

These parameters enable us to define the dimensionless parameters marked with a tilde:

- Dimensionless time, space and velocity, respectively,

$$\tilde{t} = v_{e,i}t, \quad \tilde{x} = x/\lambda_{e,i}, \quad \tilde{v} = v/v_{th}. \tag{39}$$

- Dimensionless electric field, magnetic field and distribution function, respectively,

$$E = \frac{eE}{m_e v_{th} v_{e,i}}, \quad B = \frac{eB}{m_e v_{e,i}} = \frac{\omega_{ce}}{v_{e,i}}, \quad \tilde{f}_e = f_e \frac{v_{th}^3}{n_0}. \tag{40}$$

This leads to the following dimensionless equations

$$\begin{cases} \frac{\partial f_e}{\partial t} + \nabla_\mathbf{x} \cdot (\mathbf{v} f_e) - \nabla_\mathbf{v} \cdot ((\mathbf{E} + \mathbf{v} \times \mathbf{B}) f_e) = \frac{1}{Z} C_{e,e}(f_e, f_e) + C_{e,i}(f_e), \\ \frac{\partial \mathbf{E}}{\partial t} - \frac{1}{\beta^2} \nabla_\mathbf{x} \times \mathbf{B} = \frac{1}{\alpha^2} n\mathbf{u}, \\ \frac{\partial \mathbf{B}}{\partial t} + \nabla_\mathbf{x} \times \mathbf{E} = 0, \\ \nabla_\mathbf{x} \cdot \mathbf{E} = \frac{1}{\alpha^2}(1 - n), \\ \nabla_\mathbf{x} \cdot \mathbf{B} = 0, \end{cases} \tag{41}$$

where $\alpha = v_{e,i}/\omega_{pe}$ and $\beta = v_{th}/c$. The collision terms $C_{e,e}(f_e, f_e)$ and $C_{e,i}(f_e)$ are given in (30).

6.2. 1D temperature gradient test case

In the context of laser produced plasma, the heat conduction is the leading mechanism of energy transport between the laser energy absorption zone and the target ablation zone.

In such a system, the parameters of importance for the heat flux are

- The effective electron collision mean free path λ_e.
- The electron temperature gradient length λ_T.
- The magnetic field B and its orientation with respect to ∇T.

These parameters enable to distinguish different regimes of transport, according to the Knudsen and the Hall parameters. On the one hand, the Knudsen number K_n is a measure of the thermodynamic non-equilibrium of the system

$$K_n = \frac{\lambda_e}{\lambda_T}. \tag{42}$$

A regime characterized by $K_n \to 0$ refers to an hydrodynamic limit, whereas a regime characterized by $K_n \geqslant 1$ refers to a kinetic limit, where nonlocal phenomena occur. Let us note that typical parameters for ICF yield that $K_n \geqslant 0.1$, while the hydrodynamic regime (or local approach) fails at $K_n \geqslant 0.01$. This premature failure of the local approach in plasma is explained by a specific dependence of the electron mean free path on the electron energy. In our applications the energy is transported by the fastest electrons, which have a much longer mean free path.

On the other hand, the Hall parameter $\chi = \omega_c \tau$ quantifies the relative importance of magnetic and collisional effects. $\omega_c = eB/m_e$ is the electron cyclotron frequency and τ the mean electron–ion collision time

$$\tau = \frac{12\pi^2\epsilon_0^2\sqrt{m_e}T_e^{3/2}}{\sqrt{2\pi}n_i Z^2 e^4 \ln \Lambda}. \tag{43}$$

The aim of this section is to validate our solver in different regimes, in order to show its robustness with respect to the variations of the Knudsen and Hall parameters. Thus, we consider a simple gradient temperature configuration, shown in Fig. 6, modelling a layer of homogeneous plasma. A laser deposits its energy on the hot temperature side and the absorbed energy is transported with electrons to the cold temperature side. A heat flux is created, contributing to preheating (with the fastest particles) of the region down the temperature gradient, and to smoothing of this temperature gradient. The charge separation induced by the movement of particles generates electric currents and electric fields. The heat flux and electric field are important in a preliminary transient phase. Latter in time they decrease and stabilize due to the collisional effect and the return current of cold particles. These quantities may be inhibited in the direction of the temperature gradient if the magnetic field, constant in the domain, is present. In that case, heat fluxes and electric fields are created also in the direction perpendicular to the temperature gradient. A Knudsen boundary layer is observed, having the extension of several collision mean free paths. It is due to the zero boundary current condition, where the populations that leave and enter the computational domain have different temperatures. However, since the boundaries are far enough from the temperature gradient,
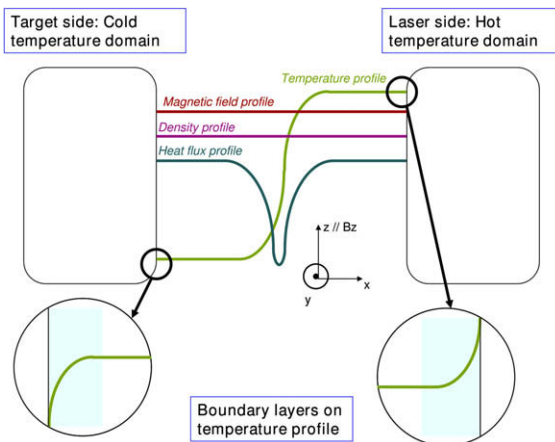
Fig. 6. Initial configuration for the temperature gradient test case: a temperature profile is considered between to two domains of plasma with particles at a thermodynamical equilibrium. Zero current boundary conditions enable to maintain the mass conservation. A heat flux is generated wherever there is a nonzero temperature gradient, as well as boundary layers on the heat flux, temperature and electromagnetic profiles.

this boundary layer does not influence the heat flux propagation in the region of the temperature gradient. We observed that the presence of a strong magnetic field enforces the variation of the fluxes inside this boundary layer.

6.3. Test 3: electron transport in the local regime

Here, we consider configurations that present small Knuden parameters: $K_n \ll 1$. In order to validate the numerical scheme in the local regime, we compare the heat flux $\mathbf{Q_{FP}}$ and electric field $\mathbf{E_{FP}}$ computed from the numerical solution of (41), with those analytically computed from an hydrodynamic model [6,36].

6.3.1. Hydrodynamic model

Let us define the average over velocity of a function $A(\mathbf{v})$

$$\langle A \rangle = \frac{1}{n_e} \int_{\mathbb{R}^3} A(\mathbf{v}) f(\mathbf{v}) \mathbf{dv}, \tag{44}$$

where $n_e(t, \mathbf{x}) = \int_{\mathbb{R}^3} f(t, \mathbf{x}, \mathbf{v}) \mathbf{dv}$ is the density of electrons.

Following [6,36], we introduce the macroscopic quantities

$$\begin{cases} \mathbf{j} = q_e n_e \langle \mathbf{v} \rangle, \\ \mathbf{q} = \frac{1}{2} m_e n_e \langle (\mathbf{v} \cdot \mathbf{v}) \mathbf{v} \rangle, \\ \mathbf{R} = \int_{\mathbb{R}^3} m_e \mathbf{v} C_{e,i}(f_e) \mathbf{dv}, \end{cases} \tag{45}$$

and

$$\begin{cases} p = n_e T_e = \frac{1}{3} m_e n_e \langle (\mathbf{v} - \langle \mathbf{v} \rangle) \cdot (\mathbf{v} - \langle \mathbf{v} \rangle) \rangle, \\ \mathbf{\Pi} = \frac{1}{3} m_e n_e \langle (\mathbf{v} - \langle \mathbf{v} \rangle) \otimes (\mathbf{v} - \langle \mathbf{v} \rangle) \rangle - p\mathbf{I}, \\ \mathbf{q_{loc}} = \frac{1}{2} m_e n_e \langle [(\mathbf{v} - \langle \mathbf{v} \rangle) \cdot (\mathbf{v} - \langle \mathbf{v} \rangle)](\mathbf{v} - \langle \mathbf{v} \rangle) \rangle, \end{cases} \tag{46}$$

where $\mathbf{j}$ is the electric current, $\mathbf{q}$ the total heat flow, $\mathbf{R}$ the friction force accounting for the transfer of momentum from ions to electrons in collisions, T_e is the temperature, p is the scalar intrinsic pressure, $\mathbf{\Pi}$ is the stress tensor, $\mathbf{q_{loc}}$ is the intrinsic heat flow and $\mathbf{I}$ the unit diagonal tensor.

Quantities p, $\mathbf{\Pi}$ and $\mathbf{q_{loc}}$ are defined in the local reference frame of the electrons, whereas $\mathbf{j}$, $\mathbf{q}$ and $\mathbf{R}$ are defined relative to the ion center of mass frame. Ions are supposed to be at rest. We have the relation

$$\mathbf{q_{loc}} = \mathbf{q} + \mathbf{j} \cdot \frac{5p\mathbf{I} + 2\mathbf{\Pi}}{2n_e e} + \mathbf{j} \frac{m_e n_e \langle \mathbf{v} \rangle^2}{2n_e e}. \tag{47}$$

The validation of our Fokker–Planck–Landau solver in the domain close to the hydrodynamic regime (local regime) requires knowledge of the transport coefficients. Following the formalism of Braginskii [6] for the transport relations, the transport coefficients in the hydrodynamic regime have been calculated by Epperlein [36]. These coefficients α_{ep}, β_{ep}, κ_{ep}, are the electrical resistivity, thermoelectric and thermal conductivity tensors, respectively. From these quantities, we are able to compare the heat flux and the electric field issued from the Fokker–Planck solver to those calculated analytically in [36], in the local regime.

The classical derivation procedure to obtain the transport coefficients involves the linearization of the Fokker–Planck–Landau equation, assuming the plasma to be close to the thermal equilibrium. The distribution function is approximated using a truncated Cartesian tensor expansion

$$f(t, \mathbf{x}, \mathbf{v}) = f^{(0)}(\|\mathbf{v}\|^2) + \frac{\mathbf{v}}{\|\mathbf{v}\|} \cdot \mathbf{f}^{(1)}(t, \mathbf{x}, \|\mathbf{v}\|).$$

Following [36], $\mathbf{\Pi}$ and $m_e n_e \langle \mathbf{v} \rangle^2$ are neglected and we consider appropriate velocity moments of $\mathbf{f}^{(1)}$, electric fields and heat fluxes are expressed as a function of thermodynamical variables. The coefficients of proportionality, in the obtained relations, are defined as the transport coefficients. Several notations can be used, depending on the chosen thermodynamical variables. Adopting the Braginskii notations, we obtain

$$\begin{cases} \mathbf{R} = \nabla p + e n_e \mathbf{E} - \mathbf{j} \times \mathbf{B} = \frac{\alpha_{ep} \cdot \mathbf{j}}{n_e e} - \boldsymbol{\beta}_{\mathbf{ep}} \cdot \nabla T_e, \\ \mathbf{q} = -\frac{5}{2} \frac{\mathbf{j}}{e} T_e - \boldsymbol{\kappa}_{\mathbf{ep}} \cdot \nabla T_e - \boldsymbol{\beta}_{\mathbf{ep}} \cdot \mathbf{j} \frac{T_e}{e}. \end{cases} \tag{48}$$

We want to compare of the results of the solver with the analytical electric fields and heat fluxes in the local regime. For that purpose, we use the values of coefficients, for $Z = 1$, that are tabulated in [36]. As for the components of these tensors, we make use of the standard notations $\|$, $\perp$ and $\wedge$. Directions denoted with $\|$ and $\perp$ are respectively parallel and perpendicular to the magnetic field. Consequently, the parallel and perpendicular components of a vector $\mathbf{u}$ are respectively $u_{\|} = \mathbf{b}(\mathbf{u} \cdot \mathbf{b})$ and $u_{\perp} = \mathbf{b} \times (\mathbf{u} \times \mathbf{b})$, where $\mathbf{b}$ is the unit vector in the direction of the magnetic field. The direction defined by the third direction in a direct orthogonal frame is denoted by $\wedge$. In the system (48), the relation between any transport coefficient tensor $\boldsymbol{\varphi}$ and vector $\mathbf{u}$ is defined by

$$\boldsymbol{\varphi} \cdot \mathbf{u} = \varphi_{\|} \mathbf{b}(\mathbf{b} \cdot \mathbf{u}) + \varphi_{\perp} \mathbf{b} \times (\mathbf{u} \times \mathbf{b}) \pm \varphi_{\wedge} \mathbf{b} \times \mathbf{u} \tag{49}$$

where the negative sign applies only in the case $\boldsymbol{\varphi} = \boldsymbol{\alpha}_{\mathbf{ep}}$.

These coefficients can be expressed in dimensionless form

$$\begin{cases} \boldsymbol{\alpha}_{\mathbf{ep}}^{\mathbf{c}} = \boldsymbol{\alpha}_{\mathbf{ep}} \frac{\tau}{m_e n_e}, \\ \boldsymbol{\beta}_{\mathbf{ep}}^{\mathbf{c}} = \boldsymbol{\beta}_{\mathbf{ep}}, \\ \boldsymbol{\kappa}_{\mathbf{ep}}^{\mathbf{c}} = \boldsymbol{\kappa}_{\mathbf{ep}} \frac{m_e}{n_e \tau T_e}. \end{cases} \tag{50}$$

The dimensionless transport coefficients $\boldsymbol{\alpha}_{\mathbf{ep}}^{\mathbf{c}}$, $\boldsymbol{\beta}_{\mathbf{ep}}^{\mathbf{c}}$, $\boldsymbol{\kappa}_{\mathbf{ep}}^{\mathbf{c}}$ are functions of Z and the Hall parameter $\chi = \omega_c \tau$ only.

The heat flux and the electric field in (48) can then be rewritten in terms of dimensionless quantities, for the particular 1D geometry of our temperature gradient configuration. In that case, the scaling using a collision frequency (38)–(40) is used:

$$\begin{cases} q_1 = -\frac{5}{2} T_e n_e^{-1} j_1 - \chi T_e B_3^{-1} \nabla_{x_1} T_e \boldsymbol{\kappa}_{\mathbf{ep},\perp}^{\mathbf{c}} - T_e \left(\boldsymbol{\beta}_{\mathbf{ep},\perp}^{\mathbf{c}} j_1 - \boldsymbol{\beta}_{\mathbf{ep},\wedge}^{\mathbf{c}} j_2 \right), \\ q_2 = -\frac{5}{2} T_e n_e^{-1} j_2 - \chi T_e B_3^{-1} \nabla_{x_1} T_e \boldsymbol{\kappa}_{\mathbf{ep},\wedge}^{\mathbf{c}} - T_e \left(\boldsymbol{\beta}_{\mathbf{ep},\perp}^{\mathbf{c}} j_2 + \boldsymbol{\beta}_{\mathbf{ep},\wedge}^{\mathbf{c}} j_1 \right), \\ E_1 = n_e^{-1} j_2 B_3 - n_e^{-1} \nabla_{x_1} p - \nabla_{x_1} T_e \boldsymbol{\beta}_{\mathbf{ep},\perp}^{\mathbf{c}} + n_e^{-1} B_3 \chi^{-1} \left(\boldsymbol{\alpha}_{\mathbf{ep},\perp}^{\mathbf{c}} j_1 + \boldsymbol{\alpha}_{\mathbf{ep},\wedge}^{\mathbf{c}} j_2 \right), \\ E_2 = -n_e^{-1} j_1 B_3 - \nabla_{x_1} T_e \boldsymbol{\beta}_{\mathbf{ep},\wedge}^{\mathbf{c}} + n_e^{-1} B_3 \chi^{-1} \left(\boldsymbol{\alpha}_{\mathbf{ep},\perp}^{\mathbf{c}} j_2 - \boldsymbol{\alpha}_{\mathbf{ep},\wedge}^{\mathbf{c}} j_1 \right). \end{cases} \tag{51}$$

The Hall parameter χ is expressed in terms of the dimensionless quantities B_3 and T_e:

$$\chi = \frac{3\sqrt{\pi}}{2\sqrt{2}} \frac{B_3 T_e^{3/2}}{Z}. \tag{52}$$

We denote by $\mathbf{Q}_{\mathbf{BR}}$ the heat flux and by $\mathbf{E}_{\mathbf{BR}}$ the electric field computed from the system (51). The transport coefficients $\boldsymbol{\alpha}_{\mathbf{ep}}$, $\boldsymbol{\beta}_{\mathbf{ep}}$, $\boldsymbol{\kappa}_{\mathbf{ep}}$ have been tabulated in [36] and will be compared with those obtained by our numerical solution approaching the kinetic FPL equation (41).

Let us note that in this configuration source terms can be considered stiff; the discretization of the collision operator is then of crucial importance and its accuracy can be tested. Moreover we provide, in this local regime, with validation results for a wide range of Hall parameters corresponding to ICF applications.

The initial temperature gradient $T_e(x_1)$ has the form of a step

$$T_e(x_1) = \begin{cases} T_e^R(x_1) & \text{if } x_1 > x_1^m, \\ T_e^L(x_1) & \text{else}, \end{cases} \tag{53}$$

where T_e^R and T_e^L are third order polynomials in $x_1 - x_1^m$, x_1 standing for the space coordinate and x_1^m for the mid-point of the 1D domain. The coefficients of these polynomials are chosen such as they verify the following conditions at x_1^m

$$\begin{cases} \frac{\partial T_e^L}{\partial x_1}(x_1^m) = \frac{\partial T_e^R}{\partial x_1}(x_1^m) = \frac{T_R - T_L}{(x_1^R - x_1^L)/\lambda}, \\ T_e^L(x_1^m) = T_e^R(x_1^m) = \frac{T_R + T_L}{2}, \end{cases} \tag{54}$$

and at the boundaries

$$
\begin{cases}
T_e^L(\overline{x_1^L}) = T_L,\\
T_e^R(\overline{x_1^R}) = T_R,\\
\frac{\partial T_e^L}{\partial x_1}(\overline{x_1^L}) = \frac{\partial T_e^R}{\partial x_1}(\overline{x_1^R}) = 0,
\end{cases}
\tag{55}
$$

where T_L (resp. T_R) is the initial temperature of the leftmost (resp. rightmost) point x_1^L (resp. x_1^R) of the domain. Here, λ is a parameter that determines the initial stiffness of the temperature gradient.

The simulations are performed with the following parameters: the size of the dimensionless domain $L = x_1^R - x_1^L = 5400$, $2 \times v_{max} = 12$, the ion charge $Z = 1$, the frequency ratio $v_{e,i}/\omega_{pe} = 0.01$, the electron thermal velocity such as $v_{th}/c = 0.05$. The magnetic field is found from the Maxwell equations; the initial values are $B_3(t = 0, x_1) = 0.001$, 0.01, 0.1 or 1. In the test cases in the local regime, any variation to this initial value proved to be negligible. The initial electric field is zero over the domain: $E_1(t = 0, x_1) = E_2(t = 0, x_1) = 0$. The initial distribution function is a Maxwellian function depending on the local temperature, with a density that is constant over the domain. The initial temperature profile is chosen such as $T_L = 0.8$, $T_R = 1.2$ and $\lambda = 10$. This set of parameters enables us to consider the local regime, close to the hydrodynamic limit (the Knudsen number is about 1/500). The second order scheme is used for the transport terms in the x_1, v_1, v_2 and v_3 directions. The dimensionless time step and mesh size are $\Delta t = 1/500$, $\Delta x_1 = L/126$, $\Delta v = 2v_{max}/32$, respectively. The grid has 126 points in space and 32^3 points in velocity; 42 processors were used for each simulation (CEA-CCRT-platine facility). The domain decomposition on the space domain allows each processor to deal only with 3 points in space. The fourth order scheme is used for the space and velocity transport terms. The zero current boundary condition is written explicitly in Section 3.4. The boundary conditions for fields are chosen with ghost points at their initial value (zero for the electric field and 0.001, 0.01, 0.1 or 1 for the magnetic field). The results are presented in Figs. 7–9. The typical run time is 24 h for 40 collision times, with that set of parameters. The maximum difference between the numerical and the analytical solution is less than 10% for longitudinal macroscopic quantities (heat flux and electric field); 20% for transverse ones. Transverse quantities have only been considered for simulations presented in Figs. 8 and 9 where the magnetic field was strong enough so that

- The transverse heat flux can attain its asymptotic value during the simulation time.
- Transverse quantities have the value comparable to the longitudinal ones.

These conditions are fulfilled for $B_3 = 0.1$, 1.

In Figs. 7–9, the results for simulations with $B_3 = 0.001$, $B_3 = 0.1$, $B_3 = 1$ are shown, respectively. The simulation with $B_3 = 0.01$ proved to show no significant differences with those with $B_3 = 0.001$.

The numerical results are shown Figs. 7–9: a transient phase is observed before attaining a stationary regime. The oscillations are enforced by the magnetic field as it is observed in Fig. 9, whereas the oscillations of electric fields are the signature of the plasma waves excited by the initial conditions. Then, these oscillations are damped in a few electron–ion collision times. These plasma oscillations are smoothed out by the large time steps we used in simulations, permitted by the implicit treatment of the Maxwell equations. However, these oscillations have a little importance on the asymptotic values and a little importance for accuracy. With a larger magnetic field, Fig. 9, we observe frequency modulations at $\omega_c = v_{e,i}$ (corresponding to $B_3 = 1$), both in electric fields and heat fluxes. The total energy is conserved with a 0.1% accuracy in the case $B_3 = 0.001$, and with a 1% accuracy with $B_3 = 1$. The total density is conserved with accuracy of 0.01%.
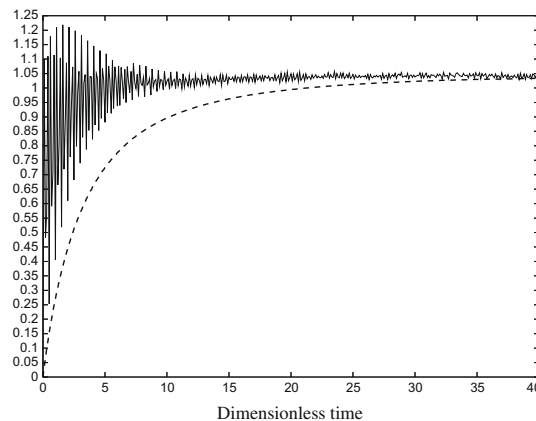

Fig. 7. The longitudinal (along the temperature gradient) heat flux ratio $\frac{\max_{x_1}(Q_{FP})}{\max_{x_1}(Q_{BR})}$ (dashed curve) and electric field ratio $\frac{\max_{x_1}(E_{FP})}{\max_{x_1}(E_{BR})}$ (oscillating curve) are shown against the dimensionless time. The dimensionless magnetic field is $B_3 = 0.001$. Asymptotic behavior, where the flux is well established, shows good agreement (less than 5% error) with analytical solution (Braginskii formalism), denoted by subscript BR.
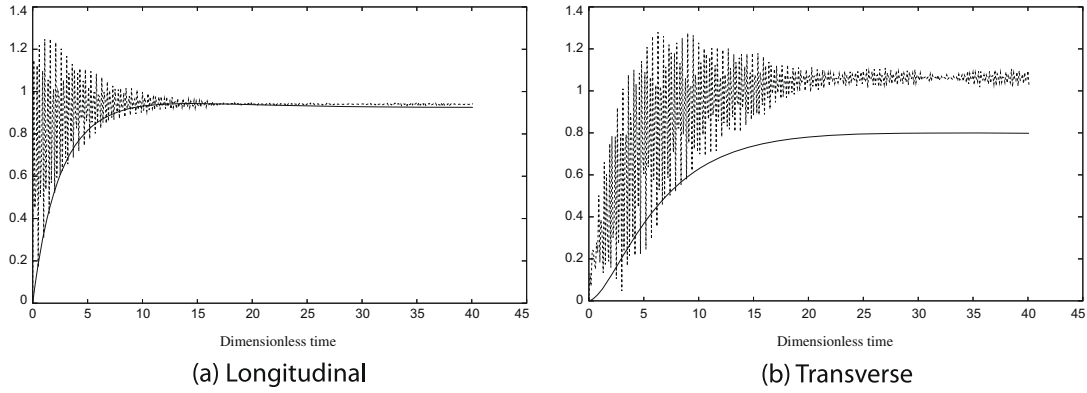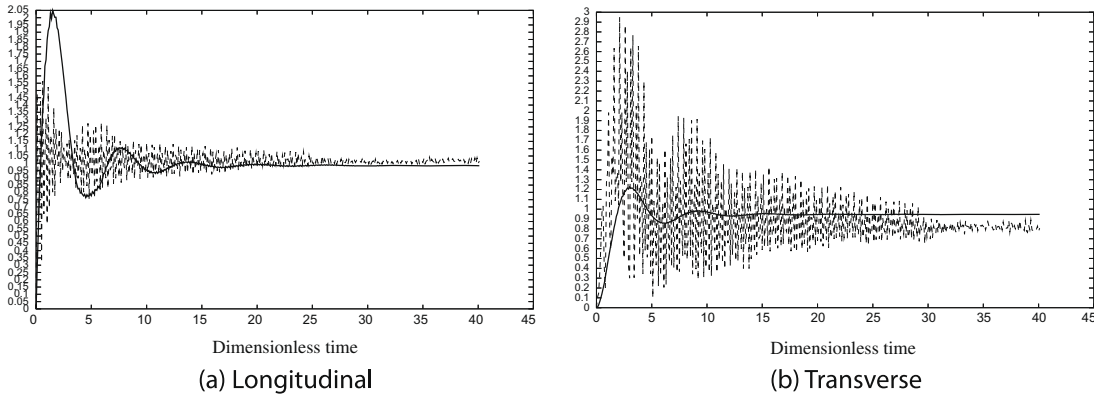
Fig. 8. Longitudinal (a) and transverse (b) heat flux $\frac{\max_{x_1}(Q_{FP})}{\max_{x_1}(Q_{BR})}$ (curve in bold) and electric field $\frac{\max_{x_1}(E_{FP})}{\max_{x_1}(E_{BR})}$ (dashed curve) are shown against the dimensionless time. Longitudinal quantities (along the temperature gradient) agree with the theoretical values with about 10% accuracy in the asymptotics. Transverse quantities agree with the theory with about 20% accuracy in the asymptotics. The dimensionless magnetic field is $B_3 = 0.1$.

Fig. 9. Longitudinal (a) and transverse (b) heat flux $\frac{\max_{x_1}(Q_{FP})}{\max_{x_1}(Q_{BR})}$ (curve in bold) and electric field $\frac{\max_{x_1}(E_{FP})}{\max_{x_1}(E_{BR})}$ (dashed curve) are shown against the dimensionless time. Longitudinal quantities (along the temperature gradient) agree with the theoretical values with about 5% accuracy in the asymptotics. Transverse quantities agree with the theory with about 20% accuracy in the asymptotics. The dimensionless magnetic field is $B_3 = 1$.

In order to investigate Larmor rotation effects for simulations presented in Figs. 8 and 9, we refined the space grid below the dimensionless Larmor radius $r_L = B_3^{-1}$. Thus the simulation presented in Fig. 8 was repeated with the same parameters on the same time period: we have refined the grid to 1260 points in space (420 processors). In the same manner, the simulation presented in Fig. 9 has been repeated with 6300 grid points in space (2100 processors) and $\Delta t = 1/1000$ (according to the CFL condition), during the same time period. The results prove to be similar to those with coarse space grids, both for macroscopic quantities and for the distribution functions. Thus no dependence on the Larmor radius is found. We recall here that the cyclotron period is always resolved, as the time steps are constrained by the CFL condition on the collision operators. The positivity property is always maintained.

6.4. Test 4: electron transport in the nonlocal regime without magnetic fields

Here, we consider configurations that present Knudsen parameters up to $K_n \simeq 1$. Therefore, we observe the behavior of the transport coefficients far from the hydrodynamic regime. These coefficients are normalized with the coefficients in the Spitzer–Härm regime, denoted by the subscript SH. The Spitzer–Härm regime is the hydrodynamic regime, with a zero magnetic field. Then it is possible to evaluate directly the ratio of effective thermal conductivity to the Spitzer–Härm conductivity, κ/κ_{SH}, by the relation:

$$\frac{\kappa}{\kappa_{SH}} = \frac{q_1}{q_{SH}}, \tag{56}$$

where q_1 is the heat flux in the x_1 direction. It is calculated from the numerical solution and q_{SH} from (51) in the Spitzer–Härm limit.

Transport coefficients are extracted from the domain where the flux and temperature gradient attain their maximum values. The effective Knudsen number, characterized by the wavelength of the temperature perturbation $k\lambda_{e,i}$ in the Fourier

space, is computed from the gradient temperature profile. This enables us to evaluate a range for $k\lambda_{e,i}$ (due to an uncertainty for the estimation of $k\lambda_{e,i}$ in the $1D_{\mathbf{x}}$ space), corresponding to this temperature gradient. The results are compared with the analytical formula from [37]

$$\frac{\kappa}{\kappa_{SH}} = \frac{1}{1 + (30k\lambda_{e,i}\beta)^{4/3}},$$ (57)

$$\beta = \left(\frac{3\pi}{128}\frac{3.2(0.24 + Z)}{(1 + 0.24Z)}\right)^{1/2}\frac{Z^{1/2}}{2}.$$ (58)

This formula has been obtained by a fit of data issued from the Fokker–Planck solver SPARK [37]. While considering the comparison between the numerical results and the analytical solution shown in Table 1, one should keep in mind that the test procedure involves a large domain of uncertainty. Three runs have been performed with the same precision for the temperature gradient. The CFL conditions are respected, maintaining the positivity of the distribution function.

6.5. Test 5: electron transport in the nonlocal regime perpendicularly to the magnetic field

The objective of this section is to illustrate a competition between the nonlocal and magnetic effects on the distribution function. More precisely, we consider a situation where the Knudsen number $K_n \simeq 1/10$. This corresponds to a situation with a stiffness parameter $\lambda = 100$. The 1D domain goes from 0 to $L = 540$, the grid has 1260 points in space, 420 processors were used for each simulation (10 collision times), during 6 h. Other parameters are kept identical to those in the test cases in the local regime. Two cases are distinguished, respectively, with weak magnetic fields effects, $\omega_c/v_{ei} = 10^{-2}$ (see Figs. 11 and 12(a)), and strong magnetic fields effects, $\omega_c/v_{ei} = 1$ (see Figs. 10(b) and 12(b)). The magnetic field is calculated from the Maxwell equations; no more than 0.1% departure from their initial value is encountered after 10 collision times. The positivity of the distribution function is maintained, and the CFL conditions are satisfied. In Figs. 10 and 11, the averaged distribution function is shown in the region of the temperature gradient

Table 1
Comparison between the numerical results and the analytical solution.

	RUN1	RUN2	RUN3
Parameters			
Size of the domain	5400	540	540
Stiffness parameter λ	10	10	100
Number of points along the gradient	126	126	1260
Number of processors	42	42	420
Results			
$k\lambda_{e,i}$	10^{-3}	0.05 ± 0.03	0.2 ± 0.1
Analytical κ/κ_{SH}	0.998	[0.93–0.67]	[0.60–0.26]
Numerical κ/κ_{SH}	1.03	0.675	0.395

$(a)\ \ t\nu_{ei} = 0$

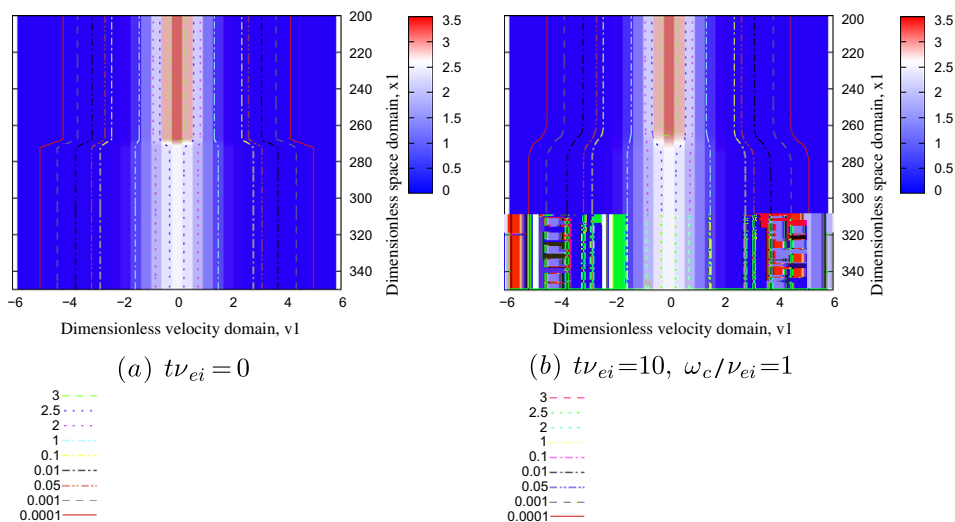$(b)\ \ t\nu_{ei} = 10,\ \ \omega_c/\nu_{ei} = 1$

Fig. 10. Averaged distribution function in the v_2 and v_3 directions, in the region of the temperature gradient, at initial time (a), and at $t\nu_{ei} = 10$ (b), for a simulation with $\omega_c/v_{ei} = 1$.

$$\sum_{j_2 j_3} f_e(t, x_1, v_{j_1}, v_{j_2}, v_{j_3}).$$

The initial distribution function, Fig. 10(a), is a Maxwellian function with a temperature that depends on the space variable x_1. It is symmetric in the v_1 direction. After 10 collision times, for the simulation with $\omega_c/v_{ei} = 10^{-2}$, Fig. 11, the distribution function keeps the same structure for the bulk electrons. Only the structure for the fastest electrons is modified. The fast electron population with positive velocities is depleted in the hot side of the temperature gradient, whereas the fast electron population with negative velocities is enforced, contributing to smoothing of the temperature gradient and heating of the bulk. These nonlocal effects are important, because the main contribution to the heat flux comes from the fastest particles.

The same distribution function is shown in Fig. 10(b), at the same time, but for a simulation with a strong magnetic field $\omega_c/v_{ei} = 1$. The distribution function is here stronger localized. This means that the magnetic field tends to inhibit the electron transport, while forcing the Larmor rotation of electrons.

In order to gain more insight in the processes at stake, we show in Fig. 12 the quantity

$$\sum_{j_2 j_3} [f_e(t, x_1, v_{j_1}, v_{j_2}, v_{j_3}) - f_e(t, x_1, -v_{j_1}, v_{j_2}, v_{j_3})],$$

which is odd in the variable v_{j_1}. It accounts for the asymmetries between the positive and negative velocities, along the direction v_1, and contributes to the heat flux and the current. We observe that the fast population contributes to the total current with a negative sign, whereas the bulk population contributes to the return current, with a positive sign. Comparing
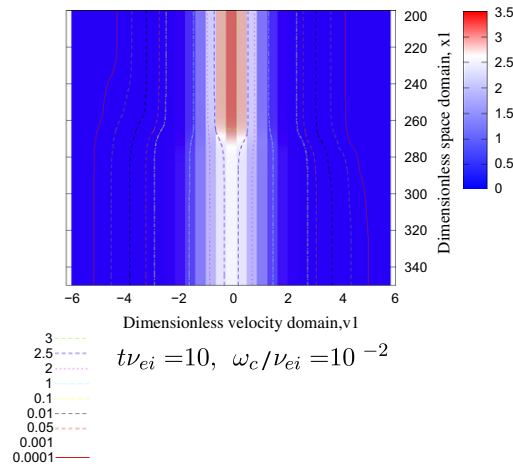

Fig. 11. Averaged distribution function in the v_2 and v_3 directions, in the region of the temperature gradient, at $tv_{ei} = 10$, for a simulation with $\omega_c/v_{ei} = 10^{-2}$.
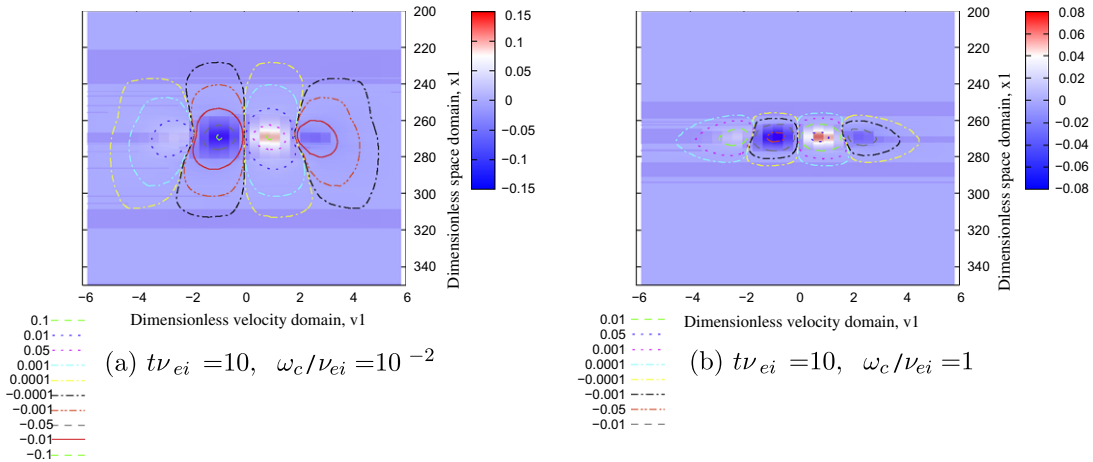

Fig. 12. The quantity $\sum_{j_2 j_3} [f_e(t, x_1, v_{j_1}, v_{j_2}, v_{j_3}) - f_e(t, x_1, -v_{j_1}, v_{j_2}, v_{j_3})]$ is shown, in the region of the temperature gradient, at the same time $tv_{ei} = 10$, for $\omega_c/v_{ei} = 10^{-2}$ in panel (a), and $\omega_c/v_{ei} = 1$ in panel (b). It corresponds to the odd part of the distribution function.

Fig. 12(a) and (b), we observe that the asymmetries are strongly re-localized in the region of the temperature gradient, with a strong magnetic field.

6.6. Test 6: 2D nonlocal magnetic field generation

We present here results on the nonlocal magnetic field generation in the relaxation of cylindrical laser hot spots, having a periodic structure, in a plasma with an initial constant density. This stands as a first step to prove the $2D_\mathbf{x}$ capabilities of the solver, and also as a comparison in the nonlocal regime with a model from the literature [39]. The extension of the present numerical schemes is straightforward on a $2D_\mathbf{x}$ grid. The fourth order scheme is used for the transport terms in the x_1, x_2, v_1, v_2 and v_3 directions.

We consider a planar geometry with periodic boundary conditions for the distribution function and fields. For this application, the scaling using a collision frequency (38)–(40) is used. The initial dimensionless temperature profile is

$$T_e(\mathbf{x}, t = 0) = 1 + 0.12 \exp\left(-\frac{\mathbf{x}^2}{R^2}\right),$$

with $R = 5.6$. We used the following parameters for the simulation: the frequency ratio is $v_{e,i}/\omega_{pe} = 0.003$, the ion charge is $Z = 5$. We do not consider here the electron–electron collision operator, because the electron–ion collisions dominate. Then the relaxation only acts with electron–ion collisions on the anisotropic part of the distribution function. The electron thermal velocity is such as $v_{th}/c = 0.05$. These parameters are close to those used in [38]. The size of the simulation domain is $L = 70$ for one space direction, $2 \times v_{max} = 12$ for one velocity direction. The initial electric and magnetic fields are zero over the domain. The initial distribution function is a Maxwellian function depending on the local temperature, the initial density being constant over the domain. The dimensionless time step and mesh size are $\Delta t = 1/500$, $\Delta x = \Delta y = L/100$, $\Delta v = 2 v_{max}/32$, respectively. The grid has 100^2 points in space and 32^3 points in velocity; 625 processors are used for this simulation. With these parameters, the CFL conditions are satisfied and the distribution function remains positive. The simulation time is 24 h.

6.6.1. First order process of temperature relaxation

The dominant process that is at play in this test case is the temperature relaxation of the hot spot. In this case the ratio *size of a hot spot/distance between hot spots* is small enough, allowing to consider, at first order, that each hot spot relaxes independently without interaction with neighbors. Therefore, we employ the $1D_x$ non-magnetized nonlocal heat transport model [39], to validate this process. This model is designed to take into account nonstationary effects, which account for the dependance of the transport coefficients on time. Two characteristic relaxation regimes are identified in [39], respectively at the hydrodynamic and collisionless kinetic time scale.

Both electron–electron and electron–ion collisions are considered in [39]. Owing the fact that we have chosen $Z = 5$, the electron–electron collisions can be considered negligible in the model [39], for this particular set of parameters.

Fig. 13 presents the evolution of the maximum of the temperature, obtained from the $2D_\mathbf{x} \times 3D_\mathbf{v}$ Maxwell–Fokker–Planck–Landau solver and from the model; it shows good agreement. The total mass is exactly preserved and the total energy is preserved with a 0.01% accuracy.

Several theoretical publications [40–43], consider configurations where magnetic field effects are important.

6.6.2. Second order process of nonlocal interaction between hot spots

The interaction between hot spots become important if the ratio *size of a hot spot/distance between hot spots* is large enough, at a given temperature perturbation. The signature of this interaction is the magnetic field generation, due to the
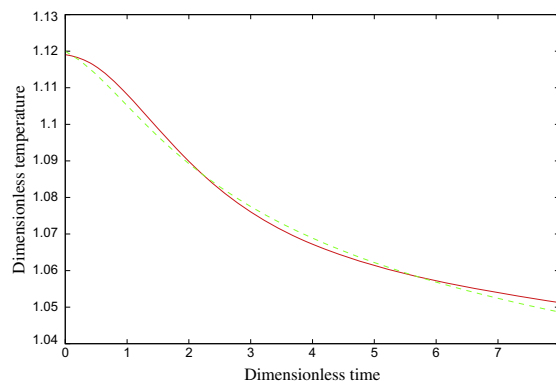

Fig. 13. Evolution of the maximum of dimensionless temperature. Comparison between the Maxwell–Fokker–Planck–Landau solver (bold, red curve) and the model from [39] (dash, green curve). (For interpretation of the references to color in this figure legend, the reader is referred to the web version of this article.)
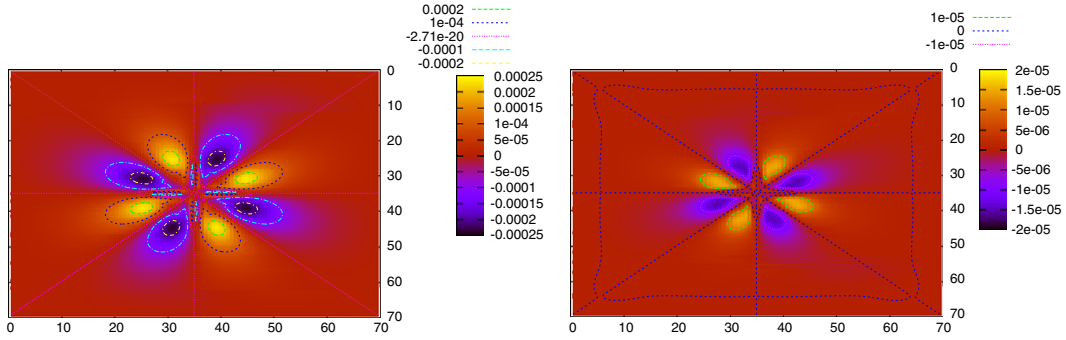
Fig. 14. Dimensionless magnetic field and cross gradients of high order moments (third and fifth) at $tv_{e,i} = 8$.

non-azimuthal symmetry, even if the density gradient is zero. This source of magnetic field cannot be described by hydrodynamic models. It is identified in [8] using a nonlocal kinetic description. A nonlocal Ohm's law that is proposed in [8] describes the magnetic field generation in plasma, at a constant density, with an isotropic pressure. A nonlocal source of magnetic field is proportional to the angle between the gradients of the third and fifth moments of the electron distribution function (see Fig. 14(b)):

$$\frac{\partial \mathbf{B}}{\partial t} \propto \nabla_{\mathbf{x}} \left(\int_{\mathbb{R}^3} f_e \|\mathbf{v}\|^3 \, \mathbf{dv} \right) \times \nabla_{\mathbf{x}} \left(\int_{\mathbb{R}^3} f_e \|\mathbf{v}\|^5 \, \mathbf{dv} \right).$$

Here the lower order term $\nabla_{\mathbf{x}} n_e \times \nabla_{\mathbf{x}} T_e$, standing as a classical source of magnetic field generation, is discarded because of the constant density.

The magnetic field and the cross gradients of high order moments are shown in Fig. 14, demonstrating a clear similarity. This test case demonstrates that our numerical method provides sufficiently high accuracy and low noise, allowing to recover the second order effects at the level better than 0.01%.

Having in view the scaling law for this mechanism with respect to the temperature perturbation [8]: $\omega_c / v_{ei} \propto (\delta T/T)^2$, we conclude that this magnetic field can influence the energy transport, if the temperature perturbation δT is large enough. Therefore, the accurate capture of high order moments by the numerical scheme is crucial for the energy transport.

7. Conclusions

In the present paper, we have developed high order numerical methods dedicated to plasma simulation at a microscopic level.

A fourth order scheme issued from VFRoe schemes has been introduced in our kinetic context. It brings accuracy improvement on the velocity transport term. The second order scheme remains interesting for the linear spatial transport term (which is faced to less robustness and accuracy constraints) in a 2D, distributed memory context without overlapping between processors (each processor communicating with its neighbours only). It involves indeed a reduced stencil, with a lower limit for the number of spatial grid points per processor.

The Maxwell equations have been discretized with a second order, implicit scheme allowing large time steps. We did not find any dependance on the Larmor radius and show that resolving the cyclotron frequency is sufficient. The couplings between the equations of the system have introduced a number of constraints (robustness, accuracy, symmetry) both on the transport scheme and the collision operators. The extension of the methods to non-uniform, cartesian grids, can be considered without affecting the conservation properties (positivity, energy, mass and momentum conservation, entropy decaying behavior). Some numerical and physical test cases have validated our approach in different regimes of interest for ICF applications, and showed that it is computationally affordable. We also proposed a validation strategy in the linear regime based on [33], using Green kernels.

Compared to other methods, the method presented here do not make any assumption on the anisotropy degree of the distribution function, neither perform simplifications on the collision operators. A distinctive feature of the present model is its flexibility. Indeed, as pointed out along this presentation, a wide range of regimes can be treated accurately with the method, from collective to collisional. Potentially, realistic, reference simulations for ICF are realizable up to hundreds of collisional times at undercritical and critical density (where collective effects are important), and at high densities (where collisional effects are dominant). The objective is to present accurate calculations, on which reduced, but faster models can rely. The counterpart of this accuracy is the computational cost of the method, despite the use of fast algorithms.

Various fundamental studies can be planned on the basis of the actual version of the solver. Collisional Weibel instability [44], forward and backward collisional Stimulated Brillouin Scattering, studies on the nonlocal interaction between speckles related to plasma-induced smoothing of laser beams [45]. Also several axis of development are under consideration to bring

more physics to the model: the ion motion, the extension to regimes relevant to higher laser intensities, including the relativistic regime and large angle collision terms of Boltzmann type.

Acknowledgments

Appendix A. Electrostatic case in the linear regime

The non-relativistic $1D_x \times 3D_{\mathbf{v}}$ Vlasov–Poisson system extracted from Eqs. (1)–(3) reads

$$\frac{\partial f}{\partial t} + v_1 \frac{\partial f}{\partial x_1} + \frac{q_e}{m_e} E_1 \frac{\partial f}{\partial v_1} = 0, \tag{59}$$

$$\frac{\partial E_1}{\partial x_1} = -\frac{q_e}{\epsilon_0} \left(n_0 - \int_{\mathbb{R}^3} f(t, x_1, \mathbf{v}) \mathbf{dv} \right). \tag{60}$$

The distribution function f is assumed to be a perturbation around an equilibrium state $f^{(0)}(\|\mathbf{v}\|)$, $E_1^{(0)} = 0$, $n_0 = \int_{\mathbb{R}^3} f^{(0)}(\|\mathbf{v}\|) \mathbf{dv}$. The system (59) and (60) is linearized around this equilibrium state

$$f(t, x_1, \mathbf{v}) = f^{(0)}(\|\mathbf{v}\|) + f^{(1)}(t, x_1, \mathbf{v}), \tag{61}$$

$$E_1^{(1)}(t, x_1) = E_1^{(0)} + E_1^{(1)}(t, x_1), \tag{62}$$

under the hypothesis:

$$\|f^{(1)}\| \ll \|f^{(0)}\|, \tag{63}$$

$$\|E_1^{(1)}\| \ll 1. \tag{64}$$

The Vlasov–Poisson can then be set under the following form (transport equation along the space directions supplemented by a source term along the v_1 direction), after linearization

$$\begin{cases} \frac{\partial f^{(1)}}{\partial t} + v_1 \frac{\partial f^{(1)}}{\partial x_1} = -\frac{q_e}{m_e} E_1^{(1)} \frac{\partial f^{(0)}}{\partial v_1}, \\ \frac{\partial E_1^{(1)}}{\partial x_1} = \frac{q_e}{\epsilon_0} \int_{\mathbb{R}^3} f^{(1)}(t, x_1, \mathbf{v}) \mathbf{dv}. \end{cases} \tag{65}$$

If $f^{(1)}$ and $E_1^{(1)}$ are periodic and integrable, then their respective normalized Fourier coefficient are well-defined. A Fourier series expansion gives $\forall t > 0$

$$\begin{cases} f^{(1)}(t, x_1, \mathbf{v}) = \hat{f}^{(1)}(t, k_1, \mathbf{v}) \cos(k_1 x_1), \\ \hat{f}^{(1)}(t, k_1, \mathbf{v}) = \frac{1}{L} \int_0^L f^{(1)}(t, x_1, \mathbf{v}) e^{-ik_1 x_1} dx_1, \end{cases} \tag{66}$$

where L is the size of the domain. The same reconstruction using Fourier series is used for $E_1^{(1)}$.

These coefficients verify the following equations, obtained by Fourier transformation performed on the equations of the system (65), for all real k_1

$$\frac{\partial \hat{f}^{(1)}}{\partial t} + ik_1 v_1 \hat{f}^{(1)} = -\frac{q_e}{m_e} E_1^{(1)} \frac{\partial f^{(0)}}{\partial v_1}, \tag{67}$$

$$ik_1 E_1 = \frac{q_e}{\epsilon_0} \hat{n}_1. \tag{68}$$

Then introducing the notation $\hat{f}^{(1)}(t = 0, k_1, \mathbf{v}) = \hat{f}^{(10)}(k_1, \mathbf{v})$, Eq. (67) can be written in the integral form

$$\hat{f}^{(1)}(t, k_1, \mathbf{v}) = \hat{f}^{(10)}(k_1, \mathbf{v}) e^{-ik_1 v_1 t} - \frac{q_e}{m_e} \int_0^t E_1^{(1)}(t', k_1) \frac{\partial f^{(0)}}{\partial v_1} e^{-ik_1 v_1 (t-t')} dt'. \tag{69}$$

Integrating Eq. (69) over $\mathbf{v}$ and injecting in it the relation (68), one obtains the following integral equation for the density

$$\hat{n}^{(1)}(t, k_1) = M(t, k_1) + \int_0^t K(t - t', k_1) \hat{n}^{(1)}(t', k_1) dt', \tag{70}$$

where

$$K(t, k_1) = \frac{iq_e^2}{k_1 m_e \epsilon_0} \int_{\mathbb{R}^3} \frac{\partial f^{(0)}}{\partial v_1} e^{-ik_1 v_1 t} \mathbf{dv}, \tag{71}$$

$$M(t, k_1) = \int_{\mathbb{R}^3} \hat{f}^{(10)}(k_1, \mathbf{v}) e^{-ik_1 v_1 t} \mathbf{dv}. \tag{72}$$

These kernels can be computed with the desired accuracy, following [33]. The numerical resolution of (70) finally reduces to the inversion of a triangular linear system.

Macroscopic quantities such as the density or the heat flux can then be reconstructed using these latter equations.

Appendix B. Initialization for the generation of a single X-mode plasma wave

This test case stands as a validation for the couplings of Vlasov and Maxwell equations. We determine initial conditions that trigger a plasma wave at a given wavelength. To do so, Vlasov–Maxwell equations are linearized, setting $f = f^{(0)} + \tilde{f}$, $E = \tilde{E}$, $B = B^{(0)} + \tilde{B}$ around the equilibrium state $f = f^{(0)}$, $E = 0$, $B = B^{(0)}$. In this appendix, we use the normalization (26)–(28). We assume periodic boundary conditions. The fluctuations of the total pressure tensor are neglected with respect to those of the magnetic field.

Using the conservation law $\frac{\partial n}{\partial t} + \frac{\partial j_1}{\partial x_1} = 0$, the former hypothesis lead us to solve the system of six equations with six unknown $\tilde{j}_1, \tilde{j}_2, \tilde{E}_1, \tilde{E}_2, \tilde{B}_3$ and $\tilde{n}$

$$
\begin{cases}
\frac{\partial \tilde{j}_1}{\partial t} + \tilde{E}_1 + B^{(0)}\tilde{j}_2 = 0, \\
\frac{\partial \tilde{j}_2}{\partial t} + \tilde{E}_2 - B^{(0)}\tilde{j}_1 = 0, \\
\frac{\partial \tilde{n}}{\partial t} + \partial_{x_1}\tilde{j}_1 = 0, \\
\frac{\partial \tilde{E}_1}{\partial x_1} = -\tilde{n}, \\
\frac{\partial \tilde{E}_2}{\partial t} = -\frac{1}{\beta^2}\frac{\partial \tilde{B}_3}{\partial x_1} + \tilde{j}_2, \\
\frac{\partial \tilde{B}_3}{\partial t} = -\frac{\partial \tilde{E}_2}{\partial x_1}.
\end{cases}
\tag{73}
$$

Applying time and space Fourier transform to this system, and identifying Fourier components ($\tilde{n} = \hat{n}\exp(-i\omega t + ik_1 x_1)$), the following system is obtain

$$
\begin{cases}
-i\omega\hat{j}_1 + \hat{E}_1 + B^{(0)}\hat{j}_2 = 0, \\
-i\omega\hat{j}_2 + \hat{E}_2 - B^{(0)}\hat{j}_1 = 0, \\
-i\omega\hat{n} + ik_1\hat{j}_1 = 0, \\
ik_1\hat{E}_1 = -\hat{n}, \\
-i\omega\hat{E}_2 = -\frac{1}{\beta^2}ik_1\hat{B}_3 + \hat{j}_2, \\
-i\omega\hat{B}_3 = -ik_1\hat{E}_2.
\end{cases}
$$

The dispersion equation of this system reads

$$
N^2 = \frac{k_1^2}{\beta^2\omega^2} = 1 - \frac{\omega^2 - 1}{\omega^2(\omega^2 - 1 - \|B^{(0)}\|^2)}.
\tag{74}
$$

In this equation, the plasma frequency is $\omega_{pe} = 1$ and the cyclotron frequency is $\omega_c = q_e\|B^{(0)}\|/m$, that is $\|B^0\|$ in this dimensionless case. The perturbation term of the distribution function at initial time can be determined for a particular solution ω of this relation dispersion. The Fourier transform is applied on the linearized Vlasov equation

$$
(-i\omega + ik_1 v_1)\hat{f} - \hat{E}_1\frac{\partial f^{(0)}}{\partial v_1} - \hat{E}_2\frac{\partial f^{(0)}}{\partial v_2} - B^{(0)}v_2\frac{\partial \hat{f}}{\partial v_1} + B^{(0)}v_1\frac{\partial \hat{f}}{\partial v_2} = 0.
\tag{75}
$$

This equation is expressed in cylindrical coordinates

$$
\begin{cases}
v_1 = v_\perp\cos(\psi), \\
v_2 = v_\perp\sin(\psi), \\
v_3 = v_\parallel,
\end{cases}
$$

where

$$
\begin{cases}
v_\perp = (\|v_1\|^2 + \|v_2\|^2)^{1/2}, \\
\tan(\psi) = \frac{v_2}{v_1}.
\end{cases}
$$

Recalling that:

$$
\nabla_{\mathbf{v}}f = \frac{\partial f}{\partial v_\perp}\nabla_{\mathbf{v}}v_\perp + \frac{\partial f}{\partial\psi}\nabla_{\mathbf{v}}\psi + \frac{\partial f}{\partial v_\parallel}\nabla_{\mathbf{v}}v_\parallel,
$$

$$
\begin{cases}
\frac{\partial v_\perp}{\partial v_1} = \cos(\psi), \\
\frac{\partial v_\perp}{\partial v_2} = \sin(\psi), \\
\frac{\partial\psi}{\partial v_1} = -\frac{1}{v_\perp}\sin(\psi), \\
\frac{\partial\psi}{\partial v_2} = \frac{1}{v_\perp}\cos(\psi),
\end{cases}
$$

with $\nabla_{\mathbf{v}} v_{\perp} = \vec{e}_{\perp}$, $\nabla_{\mathbf{v}} v_{\psi} = \vec{e}_{\psi}$ and $\nabla_{\mathbf{v}} v_{\parallel} = \vec{e}_{\parallel}$, where $\vec{e}$ are vectors in the local basis. Setting $f^{(0)}(\|\mathbf{v}\|^2) = (2\pi)^{\frac{3}{2}} \exp\left(-\frac{\|\mathbf{v}\|^2}{2}\right)$, and writing

$$(\mathbf{v} \wedge \mathbf{B}) \cdot \nabla_{\mathbf{v}}\hat{f} = (\nabla_{\mathbf{v}}\hat{f} \wedge \mathbf{v}) \cdot \mathbf{B} = -B^{(0)}\frac{\partial f}{\partial \psi}, \quad \text{with } \mathbf{B} = (0, 0, B^{(0)}),$$

the kinetic equation (75) becomes

$$(-i\omega + ik_1 v_{\perp}\cos(\psi))\hat{f} + B^{(0)}\frac{\partial \hat{f}}{\partial \psi} + f^{(0)}(\|\mathbf{v}\|^2)v_{\perp}(E_1\cos(\psi) + E_2\sin(\psi)) = 0. \tag{76}$$

In order to solve this equation, we decompose the distribution function as a Fourier series

$$\hat{f} = \sum_{n=-\infty}^{+\infty} \hat{f}_n(v_{\perp})e^{in\psi}.$$

Then from (76),

$$\sum_{n=-\infty}^{+\infty} (-i\omega + ik_1 v_{\perp}\cos(\psi) + inB^{(0)})\hat{f}_n e^{in\psi} = -f^{(0)}(\|\mathbf{v}\|^2)v_{\perp}(E_1\cos(\psi) + E_2\sin(\psi)).$$

Multiplying this equation by $e^{im\psi}$, integrating from 0 to 2π, we obtain

$$\sum_{n=-\infty}^{+\infty} \int_0^{2\pi} e^{im\psi}(-i\omega + ik_1 v_{\perp}\cos(\psi) + inB^{(0)})\hat{f}_n e^{in\psi}\, d\psi = -f^{(0)}(\|\mathbf{v}\|^2)v_{\perp}\int_0^{2\pi} e^{im\psi}(E_1\cos(\psi) + E_2\sin(\psi))d\psi. \tag{77}$$

For $m = 0$, terms are different from zero only for $n = -1, 0, 1$. From (77) comes

$$k_1 v_{\perp}\hat{f}_{-1} - 2\omega\hat{f}_0 + k_1 v_{\perp}\hat{f}_1 = 0. \tag{78}$$

For $m = -1$,

$$ik_1 v_{\perp}\hat{f}_0 - 2i(\omega - B^{(0)})\hat{f}_1 + ik_1 v_{\perp}\hat{f}_2 = -f_0(v^2)v_{\perp}(E_1 - iE_2). \tag{79}$$

For $m = 1$,

$$ik_1 v_{\perp}\hat{f}_{-2} - 2i(\omega + B^{(0)})\hat{f}_{-1} + ik_1 v_{\perp}\hat{f}_0 = -f^{(0)}(\|\mathbf{v}\|^2)v_{\perp}(E_1 + iE_2). \tag{80}$$

The case $m = -2$ involves $\hat{f}_3$,

$$ik_1 v_{\perp}\hat{f}_1 - 2(\omega - 2B^{(0)})\hat{f}_2 + ik_1 v_{\perp}\hat{f}_3 = 0. \tag{81}$$

In the same manner the case $m = 2$ involves $\hat{f}_{-3}$,

$$ik_1 v_{\perp}\hat{f}_{-3} - 2(\omega + 2B^{(0)})\hat{f}_{-2} + ik_1 v_{\perp}\hat{f}_{-1} = 0. \tag{82}$$

In order to close the system, the components f_{-3} and f_3 are neglected, and we deduce from (78)–(82),

$$\begin{cases} -2(\omega + 2B^{(0)})\hat{f}_{-2} + ik_1 v_{\perp}\hat{f}_{-1} = 0, \\ ikv_{\perp}\hat{f}_{-2} - 2i(\omega + B^{(0)})\hat{f}_{-1} + ik_1 v_{\perp}\hat{f}_0 = -f^{(0)}(\|\mathbf{v}\|^2)v_{\perp}(E_1 + iE_2), \\ kv_{\perp}\hat{f}_{-1} - 2\omega\hat{f}_0 + k_1 v_{\perp}\hat{f}_1 = 0, \\ ik_1 v_{\perp}\hat{f}_0 - 2i(\omega - B^{(0)})\hat{f}_1 + ik_1 v_{\perp}\hat{f}_2 = -f^{(0)}(\|\mathbf{v}\|^2)v_{\perp}(E_1 - iE_2), \\ ik_1 v_{\perp}\hat{f}_1 - 2(\omega - 2B^{(0)})\hat{f}_2 = 0. \end{cases}$$

The solution of linearized Vlasov equation can be calculated

$$\begin{cases} f(t, x, v) = f^{(0)}(\|\mathbf{v}\|^2) + \sum_{n=-\infty}^{\infty} \hat{f}_n(v_{\perp})e^{-i\omega t + ik_1 x_1 + in\psi}, \\ E_1(t, x) = E_1 e^{-i\omega t + ik_1 x_1}, \\ E_2(t, x) = E_2 e^{-i\omega t + ik_1 x_1}, \\ B(t, x) = B^{(0)} + B_3 e^{-i\omega t + ik_1 x_1}. \end{cases}$$

The dispersion relation (74) provides with a particular ω. Then we obtain the following results for the construction of the initial solution,

$$f(0, x, v) = f^{(0)}(\|\mathbf{v}\|^2) + \sum_{n=-2}^{2} \hat{f}_n(v_{\perp})e^{ik_1 x + in\psi}.$$

With the expressions

$$\frac{\hat{f}_{-2}}{f^{(0)}(\|\mathbf{v}\|^2)D} = i\Big(-4\omega^3 E_1 - 4i\omega^3 E_2 + 12i\omega^2 B^{(0)} E_2 + 12\omega^2 B^{(0)} E_1 - 8\|B^{(0)}\|^2\omega E_1 + k_1^2 v_\perp^2\omega E_1 + 3ik_1^2 v_\perp^2\omega E_2$$

$$- 8i\|B^{(0)}\|^2\omega E_2 - 4ik_1^2 v_\perp^2 B^{(0)} E_2\Big)v_\perp^2 k_1,$$

$$\frac{\hat{f}_{-1}}{f^{(0)}(\|\mathbf{v}\|^2)D} = 2iv_\perp\Big(E_1 k_1^2 v_\perp^2\omega^2 + 4iB^{(0)}\omega^3 E_2 - 16\|B^{(0)}\|^3\omega E_1 - 16i\|B^{(0)}\|^3\omega E_2 + 3iE_2 k_1^2 v_\perp^2\omega^2 - 4E_1\omega^4$$

$$- 8iE_2 k_1^2 v_\perp^2\|B^{(0)}\|^2 + 2k_1^2 v_\perp^2 B^{(0)}\omega E_1 + 2ik_1^2 v_\perp^2 B^{(0)}\omega E_2 + 16E_1\|B^{(0)}\|^2\omega^2 + 16iE_2\|B^{(0)}\|^2\omega^2$$

$$+ 4B^{(0)}\omega^3 E_1 - 4iE_2\omega^4\Big),$$

$$\frac{\hat{f}_0}{f^{(0)}(\|\mathbf{v}\|^2)D} = 2iv_\perp^2 k_1\Big(16\|B^{(0)}\|^2\omega E_1 + k_1^2 v_\perp^2\omega E_1 - 4\omega^3 E_1 + 4i\omega^2 B^{(0)} E_2 - 16i\|B^{(0)}\|^3 E_2 + 2ik_1^2 v_\perp^2 B^{(0)} E_2\Big),$$

$$\frac{\hat{f}_1}{f^{(0)}(\|\mathbf{v}\|^2)D} = 2i(-2B^{(0)} + \omega)v_\perp\Big(-4ik_1^2 v_\perp^2 B^{(0)} E_2 + k_1^2 v_\perp^2\omega E_1 - 3ik_1^2 v_\perp^2\omega E_2 - 12\omega^2 B^{(0)} E_1 + 12i\omega^2 B^{(0)} E_2 - 4\omega^3 E_1$$

$$+ 4i\omega^3 E_2 - 8\|B^{(0)}\|^2\omega E_1 + 8i\|B^{(0)}\|^2\omega E_2\Big),$$

$$\frac{\hat{f}_2}{f^{(0)}(\|\mathbf{v}\|^2)D} = ik_1 v_\perp^2\Big(-4ik_1^2 v_\perp^2 B^{(0)} E_2 + k_1^2 v_\perp^2\omega E_1 - 3ik_1^2 v_\perp^2\omega E_2 - 12\omega^2 B^{(0)} E_1 + 12i\omega^2 B^{(0)} E_2 - 4\omega^3 E_1 + 4i\omega^3 E_2$$

$$- 8\|B^{(0)}\|^2\omega E_1 + 8i\|B^{(0)}\|^2\omega E_2\Big),$$

where

$$D = \omega\Big(64\|B^{(0)}\|^4 - 16k_1^2 v_\perp^2\omega^2 + 16\omega^4 + 16k_1^2 v_\perp^2\|B^{(0)}\|^2 + 3k_1^4 v_\perp^4 - 80\|B^{(0)}\|^2\omega^2\Big).$$

$k_1 v_\perp$ being small with respect to $B^{(0)}$ and ω, for this particular application ($v_\perp$ must be considered in the range where the equilibrium distribution function $f^{(0)}(\|\mathbf{v}\|^2) = (2\pi)^{\frac{3}{2}}\exp\left(-\frac{\|\mathbf{v}\|^2}{2}\right)$ does not vanish. If $B^{(0)} = 2$, $\omega \simeq 5$ and $k = 2\pi/25$, then $kv_\perp \ll B^{(0)}$, ω), the numerical powers of $k_1 v_\perp$ can be neglected compared to these terms. The solution can be written

$$\frac{\hat{f}_{-2}}{f^{(0)}(\|\mathbf{v}\|^2)D} = iv_\perp^2 k_1\Big(-4\omega^3 E_1 - 4i\omega^3 E_2 + 12i\omega^2 B^{(0)} E_2 + 12\omega^2 B^{(0)} E_1 - 8\|B^{(0)}\|^2\omega E_1 - 8i\|B^{(0)}\|^2\omega E_2\Big),$$

$$\frac{\hat{f}_{-1}}{f^{(0)}(\|\mathbf{v}\|^2)D} = 2iv_\perp\Big(4iB^{(0)}\omega^3 E_2 - 16\|B^{(0)}\|^3\omega E_1 - 16i\|B^{(0)}\|^3\omega E_2 - 4E_1\omega^4 + 16E_1\|B^{(0)}\|^2\omega^2 + 16iE_2\|B^{(0)}\|^2\omega^2$$

$$+ 4B^{(0)}\omega^3 E_1 - 4iE_2\omega^4\Big),$$

$$\frac{\hat{f}_0}{f^{(0)}(\|\mathbf{v}\|^2)D} = 2iv_\perp^2 k_1\Big(16\|B^{(0)}\|^2\omega E_1 + k_1^2 v_\perp^2\omega E_1 - 4\omega^3 E_1 + 4i\omega^2 B^{(0)} E_2 - 16i\|B^{(0)}\|^3 E_2\Big),$$

$$\frac{\hat{f}_1}{f^{(0)}(\|\mathbf{v}\|^2)D} = 2iv_\perp(\omega - 2B^{(0)})\Big(-12\omega^2 B^{(0)} E_1 + 12i\omega^2 B^{(0)} E_2 - 4\omega^3 E_1 + 4i\omega^3 E_2 - 8\|B^{(0)}\|^2\omega E_1 + 8i\|B^{(0)}\|^2\omega E_2\Big),$$

$$\frac{\hat{f}_2}{f^{(0)}(\|\mathbf{v}\|^2)D} = ik_1 v_\perp^2\Big(-12\omega^2 B^{(0)} E_1 + 12i\omega^2 B^{(0)} E_2 - 4\omega^3 E_1 + 4i\omega^3 E_2 - 8\|B^{(0)}\|^2\omega E_1 + 8i\|B^{(0)}\|^2\omega E_2\Big),$$

where

$$D = \omega(64\|B^{(0)}\|^4 + 16\omega^4 - 80\|B^{(0)}\|^2\omega^2).$$

We choose to initialize the perturbation from the amplitude of the magnetic field:

$$B_3 = A \quad \text{where } A \in [0, 1].$$

Then from the system (73) and the dispersion relation (74), we deduce the values of E_1, E_2 and thus reconstruct the $\hat{f}_i$,

$$E_1 = \frac{-iB_3\Big(\omega^4\beta^2 - \omega^2 k_1^2 - \omega^2\beta^2 - \|B^{(0)}\|^2\omega^2\beta^2 + \|B^{(0)}\|^2 k_1^2\Big)}{k_1\beta^2 B^{(0)}}, \quad E_2 = \frac{\omega B_3}{k_1}.$$

References

[1] J.J. Santos et al, Fast-electron transport and induced heating in aluminium foils, Phys. Plasma 14 (2007) 103107.
[2] A.R. Bell, A.P.L. Robinson, M. Sherlock, R.J. Kingham, W. Rozmus, Fast electron transport in laser-produced plasmas and the KALOS code for solution of the Vlasov–Fokker–Planck equation, Plasma Phys. Control. Fus. 48 (2006) R37–R57.
[3] M. Tabak et al, Ignition and high gain with ultrapowerful lasers, Phys. Plasma 1 (1994) 1626.
[4] A. Bret, M.-C. Firpo, C. Deutsch, Characterization of the initial filamentation of a relativistic electron beam passing through a plasma, Phys. Rev. Lett. 94 (2005) 115002.
[5] A. Bret, L. Gremillet, D. Bénisti, E. Lefebvre, Exact relativistic kinetic theory of an electron-beam-plasma system: hierarchy of the competing modes in the system-parameter space, Phys. Rev. Lett. 100 (2008) 205008.
[6] S.I. Braginskii, Reviews of Plasma Physics, vol. 1, Consultants Bureau, New York, 1965, p. 205.
[7] M.G. Haines, Magnetic-field generation in laser fusion and hot-electron transport, Can. J. Phys. 64 (1986) 912.
[8] R.J. Kingham, A.R. Bell, Nonlocal magnetic-field generation in plasmas without density gradients, Phys. Rev. Lett. 88 (2002) 045004.
[9] C.P. Ridgers, R.J. Kingham, A.G.R. Thomas, Magnetic cavitation and the reemergence of nonlocal transport in lasers plasmas, Phys. Rev. Lett. (2008) 1.
[10] D.H. Froula, J.S. Ross, B.B. Pollock, P. Davis, A.N. James, L. Divol, M.J. Edwards, A.A. Offenbaerger, D. Price, R.P.J. Town, G.R. Tyran, S.H. Glenzer, Quenching of the nonlocal electron heat transport by large external magnetic fields in a laser-produced plasma measured with imaging Thomson scattering, Phys. Rev. Lett. (2007) 98.
[11] T. Yokota, Y. Nakao, T. Johzaki, K. Mima, Two-dimensional relativistic Fokker–Planck model for core plasma heating in fast ignition targets, Phys. Plasma 13 (2006) 022702.
[12] Y. Sentoku, A.J. Kemp, Numerical method for particle simulations at extreme densities and temperatures: weighted particles, relativistic collisions and reduced currents, J. Comput. Phys. 227 (2008) 6846–6861.
[13] R.J. Kingham, A.R. Bell, An implicit Vlasov–Fokker–Planck code to model non-local electron transport in 2-D with magnetic fields, J. Comput. Phys. 194 (2004) 1–34.
[14] J. Limpouch et al, Fokker–Planck simulations of interactions of femtosecond laser pulses with dense plasmas, Laser Part. Beam 12 (1994) 101–110.
[15] F. Alouani-Bibi, M.M. Shoucri, J.-P. Matte, Different Fokker–Planck approaches to simulate electron transport in plasmas, Comput. Phys. Commun. 164 (2004) 60–66.
[16] J.-P. Matte, J. Virmont, Electron heat transport down steep temperature gradients, Phys. Rev. Lett. 49 (1982) 26.
[17] P. Degond, B. Lucquin-Desreux, An entropy scheme for the Fokker–Planck collision operator of plasma kinetic theory, Numer. Math. 68 (1994) 239–262.
[18] C. Buet, S. Cordier, Numerical analysis of conservative and entropy schemes for the Fokker–Planck–Landau equation, Numer. Anal. 36 (1999) 953–973.
[19] C. Buet, S. Cordier, P. Degong, M. Lemou, Fast algorithm for numerical, conservative and entropy approximation of the Fokker–Planck–Landau equation, J. Comput. Phys. 133 (1997) 310–322.
[20] L. Pareshi, G. Russo, G. Toscani, Fast spectral method for Fokker–Planck–Landau collision operator, J. Comput. Phys. 165 (2000) 216–236.
[21] O. Larroche, Kinetic simulations of fuel ion transport in ICF target implosions, Eur. Phys. J. D 27 (2003) 131.
[22] F. Filbet, E. Sonnendrücker, Comparison of Eulerian Vlasov solvers, Comput. Phys. Commun. 150 (3) (2003) 247–266.
[23] M. Lemou, Multipole expansions for the Fokker–Planck–Landau operator, Numer. Math. 78 (1998) 597–618.
[24] F. Filbet, L. Pareshi, Numerical method for the accurate solution of the Fokker–Planck–Landau equation in the non-homogeneous case, J. Comput. Phys. 179 (2002) 1–26.
[25] N. Crouseilles, F. Filbet, Numerical approximation of collisional plasmas by high order methods, J. Comput. Phys. 201 (2004) 546–572.
[26] Z. Xiong, R.H. Cohen, T.D. Rognlien, X.Q. Xu, A high order finite volume algorithm for Fokker–Planck collisions in magnetized plasmas, J. Comput. Phys. 227 (2008) 7192.
[27] S. Yamamoto, H. Daiguji, High order accurate upwind schemes for solving the compressible Euler and Navier–Stokes equations, Comput. Fluid 22 (1993) 259–270.
[28] C. Berthon, F. Marche, A positive preserving high order VFROE scheme for shallow water equations: a class of relaxation schemes, SIAM J. Sci. Comput. 30 (5) 2587–2612.
[29] A. Decoster, P.A. Markowich, B. Perthame, Modeling of collisions, Research in Applied Mathematics, Masson, Paris, 1997.
[30] R. Balescu, Transport Processes in Plasmas, vol. 1, Classical Transport Theory, 1988.
[31] A. Kurganov, E. Tadmor, Solution of two-dimensional riemann problems for gas dynamics without Riemann problem solvers, Numer. Method Partial Differ. 218 (2002) 584–608.
[32] B. Van Leer, Towards the ultimate conservative difference scheme. V. A second-order sequel to Godunov's method, J. Comput. Phys. 32 (1979) 101–136.
[33] C. Sartori, G.G.M. Coppa, Analysis of transient and asymptotic behavior in relativistic Landau damping, Phys. Plasma 2 (11) (1995).
[34] S. Le Bourdiec, F. de Vuyst, L. Jacquet, Numerical solution of the Vlasov–Poisson system using generalized Hermite functions, Comput. Phys. Commun. 175 (2006) 528–544.
[35] C. Buet, S. Cordier, F. Filbet, Comparison of numerical scheme for Fokker–Planck–Landau equation, ESAIM Proc. 10 (1999) 161–181.
[36] E.M. Epperlein, M.G. Haines, Plasma transport coefficients in a magnetic field by direct numerical solution of the Fokker–Planck equation, Phys. Fluid 29 (4) (1986).
[37] E.M. Epperlein, Kinetic theory of laser filamentation in plasmas, Phys. Rev. Lett. 65 (1990) 2145.
[38] V.K. Senecha, A.V. Brantov, V. Yu Bychenkov, V.T. Tikhonchuk, Temperature relaxation in hot spots in a laser-produced plasma, Phys. Rev. E 47 (1998) 1.
[39] A.V. Brantov, V.Yu. Bychenkov, W. Rozmus, Relaxation of a thermal perturbation in a collisional plasma, Plasma Phys. Rep. 32 (4) (2006) 337–343.
[40] A.V. Brantov, V.Yu. Bychenkov, et al, Linear theory of nonlocal transport in a magnetized plasma, Plasma Phys. Rep.: Phys. Plasma 10 (12) (2003) 4633–4644.
[41] B. Frolov, S.I. Krasheninnikov, R.J. Kingham, J. Edwards, Heat flux calculation in the semi-collisionless regime for substantial temperature variations including magnetic field, New J. Phys. 8 (2006) 56.
[42] Ph. D. Nicolaï, J.-L. Feugeas, G.P. Schurtz, A practical nonlocal model for heat transport in magnetized laser, Phys. Plasma 13 (2006) 032701.
[43] D. Bennaceur-Doumaz, A. Bendib, Nonlocal electron transport in magnetized plasmas with arbitrary atomic number, Phys. Plasma 13 (2006) 092308.
[44] A. Sangam, J.-P. Morreeuw, V.T. Tikhonchuk, Anisotropic instability in a laser heated plasma, Phys. Plasma 14 (2007) 053111.
[45] J.-L. Feugeas, Ph. Nicolai, X. Ribeire, G. Schurtz, V. Tikhonchuk, M. Grech, Modelling of two dimensional effects in hot spot relaxation in laser-produced plasmas, Phys. Plasma 15 (2008) 062701.